UNIVERSIDADE FEDERAL DE PERNAMBUCO
DEPARTAMENTO DE FÍSICA- CCEN
PROGRAMA DE PÓS-GRADUAÇÃO EM FÍSICA

RAÍ MACIEL DE MENEZES

NONUNIFORM VORTEX DISTRIBUTIONS IN SUPERCONDUCTORS: FROM CRITICAL STATE TO CONFORMAL CRYSTALS

Recife
2017

RAÍ MACIEL DE MENEZES

NONUNIFORM VORTEX DISTRIBUTIONS IN SUPERCONDUCTORS: FROM CRITICAL STATE TO CONFORMAL CRYSTALS

Dissertation presented to the Postgraduate program of the Physics Department of the Federal University of Pernambuco, as a partial requirement to obtain the degree of Master in Physics.

Supervisor: Prof. Dr. Clécio Clemente de Souza Silva.

Recife

2017

Catalogação na fonte
Bibliotecária Joana D'Arc Leão Salvador CRB 4-572

M543n Menezes, Raí Maciel de.
Nonuniform vortex distributions in superconductors: from critical state to conformal crystals / Raí Maciel de Menezes . – 2017.
94 f..: fig., tab.

Orientador: Clécio Clemente de Souza Silva.
Dissertação (Mestrado) – Universidade Federal de Pernambuco. CCEN. Física, Recife, 2017.
Inclui referências.

1. Supercondutividade. 2. Vórtices. 3. Cristais conformes. I. Silva, Clécio Clemente de Souza (Orientador). II. Titulo.

537.623 CDD (22. ed.) UFPE-FQ 2017-23

RAÍ MACIEL DE MENEZES

NONUNIFORM VORTEX DISTRIBUTIONS IN SUPERCONDUCTORS: FROM CRITICAL STATE TO CONFORMAL CRYSTALS

Dissertation presented to the Postgraduate program of the Physics Department of the Federal University of Pernambuco, as a partial requirement to obtain the degree of Master in Physics.

Accepted on: 06/03/2017.

EXAMINING BOARD:

Prof. Dr. Clécio Clemente de Souza Silva
Supervisor
Universidade Federal de Pernambuco

Prof. Dr. Leonardo Ribeiro Eulálio Cabral
Internal examiner
Universidade Federal de Pernambuco

Prof. Dr. Andrey Chaves
External examiner
Universidade Federal do Ceará

Agradecimentos

Ao meu orientador, Clécio, por toda paciência e dedicação.

A Camila, por todo o apoio, compreensão e incentivo imprescindíveis.

Ao meu irmão, Raniere, por tudo que ele representa como inspiração.

Aos meus pais, Geraldo e Taciana, por todo o apoio do mundo.

Aos meus amigos, Clodomir, Joás (o monstro), Lucas, Vinícius, Mario e muitos outros, pelas conversas e amizade.

Ao professor Leonardo Cabral e aos demais membros do grupo de dinâmica de vórtices da UFPE.

Aos meus professores de inglês, Manoel, Jhonny e Victor.

Aos demais membros do departamento de física da UFPE.

Às agências de fomento CAPES e CNPq .

Once you eliminate the impossible, whatever remains, no matter how improbable, must be the truth.

— Sherlock Holmes in The Sign of the Four.

- Sir. Arthur Conan Doyle.

Abstract

In this dissertation, we study through numerical simulation, properties of the vortex matter in superconductors. In non-homogeneous superconductors, the penetration of magnetic flux (provided by the vortex entry) within the sample is theoretically described by the macroscopic critical state models, where due to interaction with material impurities (pinning centres), the vortex density is high near the edges and decreases as we approach the center of the sample. Although extensively studied, the critical state models do not explain in detail how the microscopic events lead to the global behavior predicted by the macroscopic models , especially nearby the surfaces, where the vortex currents are deformed to satisfy the boundary conditions. We simulate through molecular dynamics methods the penetration and the microscopic dynamics of vortices in a superconducting slab subjected to a parallel applied magnetic field. We explicitly take into account the often neglected vortex-surface interaction and analyse how this can influence the dynamics and the critical state configurations. We then verify which of the various critical state models best describes the system. Nearby the surfaces, we observed regions with zero density of vortices, which arise due to the energetic barrier that hinders the vortex entry and exit. Such regions, known as *flux free regions*, have a thickness which depends on the strength of the applied magnetic field and the level of pinning forces in the material. We also analyse the temporal evolution of the flux front inside the superconductor and the hysteresis cycles of the magnetization due to an external field variation, and compare with results known in the literature. Another topic of broad interest concerns the possible ordered structures that the vortex lattice can form. In situations of uniform density the system of vortices converges to a minimum of energy and tends to be ordered as a triangular lattice (Abrikosov lattice). However, in situations where the vortices may form nonuniform distributions, due to variations in sample thickness, interactions with material inhomogeneities, among other ways, the triangular Abrikosov lattice will not satisfy the minimum energy condition. The question is whether the nonuniform distribution of vortices presents a structure of small domains of different densities, i.e., a nonuniform glass, or a new ordered structure emerges. We obtain evidences of conformal crystals as possible, stable nonuniform vortex configurations in a superconductor. Such configuration is an example of ordered crystallization in a nonuniform particle distribution. These ordered structures,

although can present local inhomogeneities, preserve the topological order and can be mathematically mapped into a triangular lattice through a conformal transformation. We propose a simple method to obtain the particle density required to observe such structures and suggest possible experimental realizations in which conformal (or quasi-conformal) vortex crystals could be observed in bulk superconductors or thin films.

Keywords: Superconductivity. Vortices. Critical state. Conformal crystals.

Resumo

Nesta dissertação, estudamos através de simulação computacional, propriedades da matéria de vórtices em supercondutores. Em supercondutores não homogêneos, a penetração do fluxo magnético (proporcionada pela entrada de vórtices) no interior da amostra é descrita teoricamente pelos modelos macroscópicos de estado crítico, onde devido à interação com as impurezas do material, a densidade de vórtices é alta próximo às bordas e decresce à medida que nos aproximamos do centro da amostra. Apesar de terem sido bastante estudados, os modelos de estado crítico não respondem detalhadamente qual a conexão dos eventos microscópicos com os resultados dos modelos macroscópicos, principalmente nas imediações da superfície, onde as correntes dos vórtices são deformadas para satisfazer as condições de contorno. Simulamos através de métodos de dinâmica molecular a penetração e a dinâmica microscópica de vórtices em um filme supercondutor devido à presença de um campo magnético aplicado paralelamente à sua superfície. Reproduzimos a interação dos vórtices com a superfície do supercondutor e analisamos como isso pode influenciar na dinâmica e nas configurações de estado crítico. Verificamos então qual dentre os vários modelos de estado crítico descreve melhor o sistema. Nas imediações da superfície, observamos regiões com densidade nula de vórtices, as quais surgem devido a barreira energética que retarda a entrada e a saída das linhas de fluxo no supercondutor. Tais regiões, conhecidas como *flux free regions*, têm uma espessura que depende da intensidade do campo magnético aplicado e do nível de impurezas do material. Analisamos também a evolução temporal da frente de fluxo dentro do supercondutor e os ciclos de histerese da magnetização devidos à variação de um campo magnético externo e comparamos com resultados conhecidos na literatura. Outro olhar interessante é em relação as possíveis estruturas ordenadas que a rede de vórtices pode formar. Em situações de densidade uniforme, o sistema converge para um mínimo de energia e tende a se ordenar como uma rede triangular (rede de Abrikosov). Entretanto, em situações em que os vórtices podem formar distribuições não uniformes, devido variações na espessura da amostra, interações com inomogeneidades do material, dentre outras maneiras, a rede triangular de Abrikosov não satisfará a condição de mínima energia. A questão é se a distribuição não uniforme de vórtices apresenta uma estrutura de pequenos domínios de diferentes densidades, i.e., um vidro não uniforme, ou se uma

nova estrutura ordenada emerge. Obtemos evidências da formação de cristais conformes como uma rede estável de vórtices em um supercondutor. Tal formação é um exemplo de cristalização ordenada da rede em uma distribuição de partículas não uniforme. Estas estruturas ordenadas, embora possam apresentar inomogeneidades locais, preservam a ordem topológica e podem ser matematicamente mapeadas em uma rede triangular através de uma transformação conforme. Propomos um método simples para gerar a densidade de partículas necessária para a observação de tais estruturas e sugerimos possíveis experimentos nos quais cristais conformes de vórtices, ou quase conformes, poderiam ser observados em supercondutores volumosos e filmes finos.

Palavras-chave: Supercondutividade. Vórtices. Estado crítico. Cristais conformes.

List of Figures

Contents

1 Introduction

The theory of vortices in superconductors has been exhaustively studied over the past six decades since Alexei Abrikosov (1957) demonstrated that, when subjected to sufficiently high magnetic fields, some superconducting materials are threaded by quantized flux lines, which induce circular screening currents (or **vortices** of currents) around it in order to preserve the superconductivity in the rest of the material. Such vortices interact repulsively with each other as well as interact with applied currents in the material. Abrikosov then classified the superconducting materials in two types: type-I, those materials that do not allow partial flux penetration, and type-II, materials that allow partial flux penetration and consequently the formation of vortices. The vast majority of superconductors are type-II, which makes this type of superconductor of greater technological interest. Several metal alloys and various composite systems are of this type of superconductivity, and are also present in electronic devices and medical equipments. The vortex dynamics influences directly in most physical properties of the system such as resistivity and magnetization, such that a study on the vortex matter becomes relevant for all applications.

Abrikosov also showed that the vortices that permeate a homogeneous superconductor arrange themselves in a regular lattice. We now know that, in this case, the vortices are organized in a triangular lattice. However, structural defects in the material, whether natural or artificially produced, act as attractive centres for the vortices, and are usually called *pinning centres*. The vortex-pinning interaction deforms the homogeneous lattice and is able to form disordered structures or even nonuniform vortex distributions. Other factors such as temperature and geometry of the sample also play a relevant role in the deformation of the vortex lattice.

The flux line (or vortex) dynamics in a superconductor is usually described by its two-dimensional motion on the physical plane perpendicular to the applied field direction. In some situations (e.g. for thin superconducting films or when the vortices are practically straight lines), the vortex system can be treated as pointlike particles interacting in a two-dimensional dynamics. Thus, an arrangement of vortices in a

superconductor resembles several systems of interacting particles on a substrate, e.g., colloids, plasma and Wigner crystals. In this way, a study on vortex matter may also bring solutions to problems in other areas.

In situations of nonuniform density of vortices, little is known about which structures the vortex lattice can form, especially if ordered configurations are possible or not. In this work we propose an attempt to find the so-called conformal crystals as possible minimum energy configurations for nonuniform vortex distributions. A conformal crystal is a nonuniform ordered structure in which the position of its particles can be mapped via a conformal transformation from a regular hexagonal lattice. In the following chapters we review the theory of vortices in superconductors (chapter 2) and study, through numerical simulations, situations of nonuniform vortex densities (chapter 3 and chapter 4). In chapter 3 we discuss the nonuniform vortex distributions produced by the competition between the flux penetration and the pinning force in the so-called critical state problem, where we study how the surface effects can influence on the vortex distribution. Then, in chapter 4, we model the necessary conditions to obtain the conformal vortex crystals, study the properties of this exotic configuration, and suggest the possible experimental realizations. The main conclusions of this work are summarized in chapter 5.

2 Vortex State in Superconductors

In this chapter we review some basic theories of superconductivity, starting from the first mathematical explanations of how the magnetic flux penetrates into a superconducting sample, towards describing the vortex lattice. We will discuss the types of superconductors and study how the magnetic flux can be quantized inside the material, thus forming the vortices. Then we will see how the flux lines interact with the structural defects of the superconducting crystal and how it can produce a nonuniform vortex density in the so-called critical state. Finally, we discuss the possibility of the vortex lattice be treated as a two dimensional crystal.

2.1 Historical overview

The fascinating phenomenon of superconductivity was revealed to human eyes for the first time in 1911, when the Dutch physicist Heike Kamerlingh Onnes, a pioneer in cooling techniques, having already liquefied helium in 1908 in his laboratory at Leiden University, realized that the resistance of mercury dropped to zero for temperatures below 4.15K [1]. This finding resulted in the birth of the field of superconductivity. It did not take long until other experiments were made for different materials and it was found that some of them have the same behaviour when submitted to very low temperatures. Each of them is characterized by a specific critical temperature T_c, that determines the phase transition between the normal and superconductor states.

Later, in 1913, Onnes also discovered that the superconductivity can be destroyed above a critical current density J_c [2], and subsequently, he found that there is a critical magnetic field B_c limiting the superconducting state [3]. Therefore the superconductivity occurs under the conditions $T < T_c, B < B_c, J < J_c$. But it was just in 1933 that Meissner and Ochsenfeld [4] found the second most important property of a superconductor, the total exclusion of magnetic field inside the material for temperatures below T_c, i.e., the superconductor behaves like a perfect diamagnetic, expelling the magnetic field

from inside of it. This effect, known as Meissner effect, can not be explained by a perfect conductor, which would shield the magnetic field if subjected to a magnetic flux variation, but once an internal magnetic flux has been established, this flux would not be expelled below T_c.

The first mathematical explanation of superconductivity was proposed by the brothers F. and L. London, in 1935 [5]. They proposed equations to explain the behaviour of electric and magnetic fields and current density inside a superconductor. They also predicted how far an external magnetic field can penetrate into a superconductor. The next superconductivity theory came fifteen years latter when Ginzburg and Landau formulated a successful phenomenological theory describing the superconductivity in terms of an order parameter that represents the density of super electrons (later known as cooper pairs) [6]. Particularly, other scientist Alexei Abrikosov showed that Ginzburg-Landau theory predicts the division of superconductors into two distinct groups, Type I and Type II. Type I superconductors, in the presence of an applied magnetic field, have only one phase transition between normal and Meissner states, while type II superconductors are characterized by two critical fields, which depend on temperature. In between such field values a type II superconductor manifests a peculiar state, called mixed state, where partial penetration of magnetic flux occurs, but preserving the material's superconductivity. The mixed state is characterized by the presence of superconducting vortices, which are the main subject of this work.

In 1950, the same year of the Ginzburg-Landau theory, Maxwell and Reynolds observed that the critical temperature of mercury isotopes depends on the isotopic mass. This result indicates the electron-phonon interaction as a microscopic mechanism responsible for superconductivity. This effect, called the isotope effect, was proposed theoretically by Frölich [7] in the same year and is considered an important step towards a microscopic superconductivity theory.

The BCS theory [8], proposed by Bardeen, Cooper and Schriffer (1957), brought a complete quantum microscopic explanation of superconductivity. This theory assumes that the supercurrents are carried by electron pairs, called cooper pairs. The electron-phonon interaction produces a net attractive force between the electrons which are organized in pairs and an energy gap is created between the normal and superconductor states. The BCS theory satisfactorily explains almost all the microscopic properties of elementary superconductors and it is in accordance with the London and Ginzburg-Landau results.

In this chapter we review some basic theories of superconductivity in order to describe the physics of superconducting vortices. A detailed study of the microscopic effects becomes unnecessary here, since the phenomenological theories of London and Ginzburg-Landau satisfactorily describe the dynamics of superconducting vortices.

2.2 London equations

The London equations were proposed to explain the behaviour of electromagnetic fields inside a superconductor. The first equation establishes the relation between the local eletric field, **E**, and current density, **J**, while the second one relates the current density to the local magnetic induction **B**,

$$\mathbf{E} = \mu_0 \lambda_L^2 \frac{\partial \mathbf{J}}{\partial t}, \tag{2.1}$$

$$\mathbf{B} = -\mu_0 \lambda_L^2 \nabla \times \mathbf{J}, \tag{2.2}$$

where λ_L is the London penetration depth, a phenomenological parameter that can be written as $\lambda_L = \sqrt{m^*/\mu_0 e^{*2} n_s}$, with m^*, e^* and n_s the mass, charge and density, respectively, of the superelectrons (or "superconducting carriers", known later as cooper pairs) . The first equation represents the perfect conductivity, i.e., any electric field can accelerate the superelectrons. From the Ampère's law, we can rewrite de current density as $\mu_0 \mathbf{J} = \nabla \times \mathbf{B}$. Using this expression in Eq.(2.2) we obtain

$$\nabla^2 \mathbf{B} = \frac{\mathbf{B}}{\lambda_L^2}, \tag{2.3}$$

where we also used the identity $\nabla \times \nabla \times \mathbf{B} = \nabla(\nabla \cdot \mathbf{B}) - \nabla^2 \mathbf{B}$ and Gauss' law $\nabla \cdot \mathbf{B} = 0$. Eq.(2.3) corresponds to a Helmholtz equation and has well known solutions for some symmetries.

2.2.1 Magnetic field inside superconductor

Consider an infinite superconducting film on the y-z plane of thickness d, i.e., at $-d/2 < x < d/2$, under a constant applied magnetic field in z direction $\mathbf{B} = B_0 \hat{z}$, as illustrated in Fig. 2.1. In this case the local magnetic induction must satisfy the

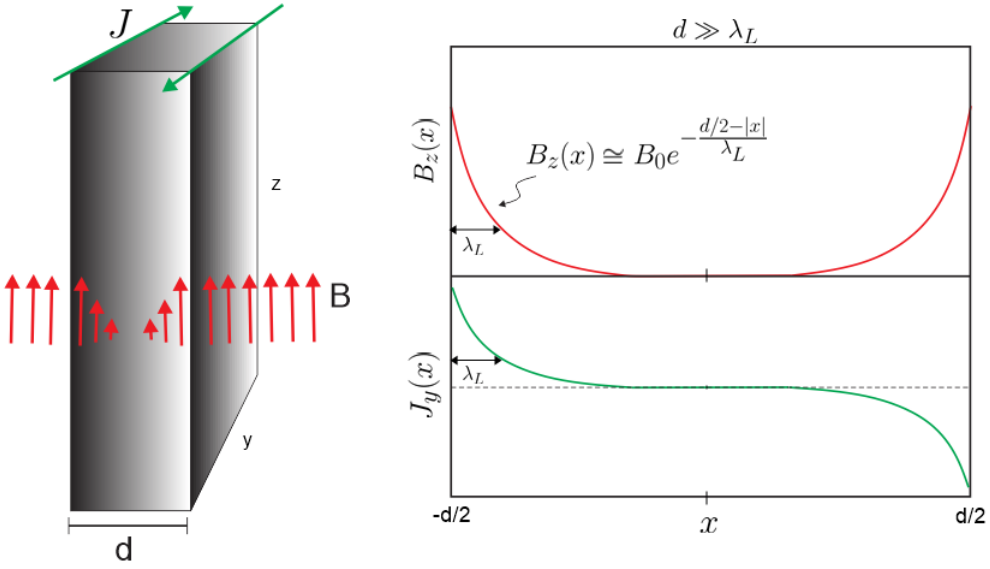

Figure 2.1: Field and current representation in the London theory for an infinite superconducting film of thickness d.

boundary conditions $B_z(x = -d/2) = B_z(x = d/2) = B_0$ and the solution to London equation becomes

$$B_z(x) = \frac{B_0 \cosh(\frac{x}{\lambda_L})}{\cosh(\frac{d}{2\lambda_L})} \quad , \quad -\frac{d}{2} < x < \frac{d}{2}. \tag{2.4}$$

Note that for $d \gg \lambda_L$ this solution is reduced to $B_z(x) = B_0 \exp(\frac{-(d/2-|x|)}{\lambda_L})$ and the magnetic field inside the superconductor decreases to zero in a characteristic length λ_L from the surface. Observe that Eq.(2.4) represents the Meissner effect.

2.2.2 *Shielding current*

The shielding current can be easily calculated from Ampere's law. For **B** in z direction we have $\mathbf{J} = -\frac{1}{\mu_0}\frac{\partial B_z}{\partial x}\hat{y}$. Using $B_z(x)$ from Eq.(2.4)

$$J_y(x) = -\frac{B_0}{\mu_0 \lambda_L}\frac{\sinh(\frac{x}{\lambda_L})}{\cosh(\frac{d}{2\lambda_L})} \quad , \quad -\frac{d}{2} < x < \frac{d}{2} \tag{2.5}$$

Thus the absolute value of current density also decrease from the surface with the same characteristic length λ_L. Note that **J** is perpendicular to the magnetic field and is oriented in a way as to shield the flux density, as illustrated in Fig. 2.1. For $d \ll \lambda_L$, the

magnetic flux penetration reaches the middle of the sample and the shielding currents surround all material, with more intensity near the surface and decreasing towards the center. Empirically, the penetration depth depends on temperature by the expression

$$\lambda_L(T) \approx \lambda_L(0) \left[1 - (T/T_c)^4\right]^{-\frac{1}{2}}. \tag{2.6}$$

Although the London theory can explain the perfect conductivity and Meissner effect, it has limitations. For example the density of superelectrons is considered uniform in all material, it does not yield the upper critical field or critical current density for superconductivity, and it does not describe the mixed state in its original form. The Ginzburg-Landau theory brought the answers to these problems, as we shall see below.

2.3 Ginzburg-Landau theory

Based on the second-order phase transition theory of Landau, the Guinzburg-Landau (GL) theory describes the macroscopic behaviour of superconductors using the total free energy of the system, contrary to the BCS theory, where the microscopic excitations are considered. Thus, the GL theory describes more easily situations in which there are spatial inomogeneities in the density of superelectrons and will be sufficient to describe the superconducting vortices. The authors introduced a pseudo wave function $\psi(\mathbf{r}) = |\psi(\mathbf{r})|e^{i\varphi(\mathbf{r})}$ as a complex order parameter, where $|\psi(\mathbf{r})|^2$ represents the density of superconducting electrons, $n_s(\mathbf{r})$. In that way the electrons are treated as a quantum fluid and, differently from the London theory, their density ,n_s, can assume non-uniform values.

At first, this theory had limited attention in the literature due to its phenomenological foundations. But, in 1959 Gor'Kov [9] showed that the GL theory derives from a particular case of the miscroscopic theory for temperatures close to T_c and with $\psi(\mathbf{r})$ varying slowly in space.

2.3.1 Order parameter

Some systems in nature can be characterized by two distinct behaviours: disordered, when subjected to high temperatures and ordered for low temperatures. The order parameter of a system is a physical parameter that can represents the transition between

these two phases. For example, in ferromagnetic materials, the magnetization can be taken as an order parameter, since it is equal to zero for high temperatures (spins randomly oriented) and is nonzero for low temperatures (aligned spins). Similarly, the superconducting order parameter might be associated to the density of superelectrons, which is zero only for temperatures above T_c. In that way, the order parameter describes the phase transition between the normal and the superconducting states.

2.3.2 *Free Energy and the Ginzburg-Landau equations*

At first, consider $|\psi(\mathbf{r})|^2$ uniform everywhere in the material for zero magnetic field, $B_{ext} = 0$. According to Landau's theory of second-order phase transitions, we can expand the free energy density of a superconductor f_s in terms of the order parameter $|\psi(\mathbf{r})|^2$

$$f_s = f_n + \alpha(T)|\psi(\mathbf{r})|^2 + \beta(T)|\psi(\mathbf{r})|^4 + \gamma(T)|\psi(\mathbf{r})|^6 + \ldots \tag{2.7}$$

As we saw above, the order parameter represents the number of electrons that condensed in the superconducting state. Then, for $|\psi(\mathbf{r})|^2 \longrightarrow 0$, Eq.(2.7) results in the free energy density of the normal state, f_n. Considering temperatures near T_c, we can approximate the expansion of Eq.(2.7) as $f_s = f_n + \alpha(T)|\psi(\mathbf{r})|^2 + \beta(T)|\psi(\mathbf{r})|^4$, where we preserved the third term in order to avoid an unique and trivial solution $\psi = 0$. The Landau's theory is summarized in finding a equilibrium state that minimizes the global Gibbs free energy, which is equal to the Helmholtz energy for zero field, $F = \int dr^3 f_s(\psi(\mathbf{r}))$. For this we make use of variational calculus to minimize the functional of energy in relation to the order parameter. This results in a expression that the parameters must satisfy at a minimum , $\alpha\psi + \beta|\psi|^2\psi = 0$. Immediately, we conclude that β must assume positive values, otherwise the energy would not have a global minimum within the domain that validates the expansion. In that way ψ assumes the possible solutions

$$\psi = 0 \quad , \quad |\psi| = \sqrt{-\frac{\alpha}{\beta}} \tag{2.8}$$

Let us now define $|\psi_\infty|^2 \equiv -\alpha/\beta$ as the value of $|\psi(\mathbf{r})|^2$ deep inside the superconductor, where the order parameter assumes an uniform value for any applied magnetic field, this will be useful later. Note that, once β is positive, $\alpha(T)$ defines the critical temperature, i.e., $\alpha > 0$ results on the unique solution $\psi = 0$, and the system stays in the normal

state, on the other hand, for $\alpha < 0$ the other solutions from Eq.(2.8) become possible and the superconductor state is energetically favorable. Empirically, $\alpha(T)$ depends on temperature by $\alpha(T) \sim (T - T_c)$. These results are analogous to the Bragg-Williams free energy for the Ising model with zero magnetic field, where the order parameter is the magnetization. A more detailed explanation can be found in (P. Chaikin et al,1995 [10]).

Let us now assume that $|\psi|$ varies slowly in space and the superconductor is under an applied magnetic field $B_{ext} \neq 0$. In this case, the GL theory adds two new terms in the free energy

$$f_s = f_n + \alpha(T)|\psi(\mathbf{r})|^2 + \beta(T)|\psi(\mathbf{r})|^4 + \frac{1}{2m^*}|[-i\hbar\nabla - e^*\mathbf{A}(\mathbf{r})]\psi(\mathbf{r})|^2 + \frac{b^2}{2\mu_0}, \tag{2.9}$$

where $\mathbf{A}(\mathbf{r})$ is the vector potential operator, that is related to the magnetic field by the expression $\mathbf{b} = \nabla \times \mathbf{A}$. The fourth term of Eq.2.9 represents the kinetic energy and can be read as $\mathbf{P}^2/2m^*$, where $\mathbf{P} = -i\hbar\nabla - e^*\mathbf{A}(\mathbf{r})$ is the physical momentum operator. The latter term represents the magnetic field energy in the vacuum. Obviously, when $\psi = 0$, the normal free energy density remains $f_n + b^2/2\mu_0$.

To derive the GL equations, we must minimize the global free energy, similar to the zero field case that we saw above, but note that now the Gibbs free energy differs from the Helmholtz free energy, integrated in the volume V, by a term as in the following expression

$$G_s[\psi, \mathbf{A}] = \int dV f_s(\psi, \mathbf{A}) - V\mathbf{H} \cdot \mathbf{B}, \tag{2.10}$$

Observe that G_s is a functional and we can minimize it by using variational calculus. We obtain the first GL equation by minimizing G_s with respect to ψ^*, i.e.,

$$\frac{\delta G_s}{\delta \psi^*} = \alpha\psi + \beta|\psi|^2\psi + \frac{1}{2m^*}(-i\hbar\nabla - e^*\mathbf{A})^2\psi = 0, \tag{2.11}$$

which is similar to the Schrödinger equation, differing only by a nonlinear term, with ψ being the wave function and α the energy eigenvalue.

In the same way, minimizing G_s with respect to $\mathbf{A}$ and simplifying algebraically the expression, we obtain the second GL equation

$$j_s = -\frac{i\hbar e^*}{2m^*}(\psi^*\nabla\psi - \psi\nabla\psi^*) - \frac{e^{*2}}{m^*}|\psi|^2\mathbf{A}. \tag{2.12}$$

These two equations can be solved to obtain the spatial variation of the order parameter and the current density of the superelectrons.

2.3.3 *Characteristic lengths*

The Ginzburg Landau theory introduces two fundamental length scales associated with superconductivity. To understand them let us consider now a normal-superconductor interface in a three-dimensional Euclidean space with $x < 0$ representing a normal material and $x > 0$ a superconductor. Assuming that there are no fields and currents applied, we can use $\mathbf{A} = 0$ in Eqs.(2.11) and (2.12), such that, all coefficients of the first GL equation become real. From the second equation we find that, in that case, $\nabla\varphi = 0$. Therefore the phase is everywhere constant and can be set to zero without changing the physics of this problem. In that way $\psi = \psi(x)$ is real and we can rewrite Eq.(2.11) in unidimensional form

$$\frac{-\hbar^2}{2m^*}\frac{d^2}{dx^2}\psi + \alpha\psi + \beta|\psi|^2\psi = 0 \tag{2.13}$$

For a homogeneous superconductor, we expected that for $x \gg 0$ the order parameter becomes uniform and the magnetic field vanish, leading us to the case $\psi^2 = \psi_\infty^2 = -\alpha/\beta$, as we saw before. We are interested here in how the order parameter differs from ψ_∞ in the non-uniform regions near the surface. For this purpose, let us rewrite the above equation in terms of the parameter $f = \psi/\psi_\infty$

$$\frac{-\hbar^2}{2m^*|\alpha|}\frac{d^2}{dx^2}f + f(1 - f^2) = 0. \tag{2.14}$$

Now, it is convenient to define the first fundamental length $\xi^2 \equiv \hbar^2/2m^*|\alpha(T)|$, known as **coherence length**. In that way, It may be easily verified that Eq.(2.14) has the solution $f(x) = \tanh(x/\sqrt{2}\xi)$. Rewriting in terms of ψ, we find.

$$\psi(x) = \psi_\infty \tanh(\frac{x}{\sqrt{2}\xi}) \tag{2.15}$$

Note that $\psi(x) \longrightarrow \psi_\infty$ when $x \gg \xi$ and $\psi(x) = 0$ at the normal-superconductor interface. Therefore, ξ determines the characteristic distance in which the order parameter vary in the transition from a superconductor to a normal region. Also note that ξ depends on temperature by $\alpha(T)$, i.e., $\xi^2(T) \simeq \xi^2(0)/(1 - T/T_c)$, which diverges for $T \longrightarrow T_c$, when the superconductivity vanishes.

The second fundamental length is related to the characteristic distance in which the magnetic field can penetrate into the superconducting region. Beforehand, let us define

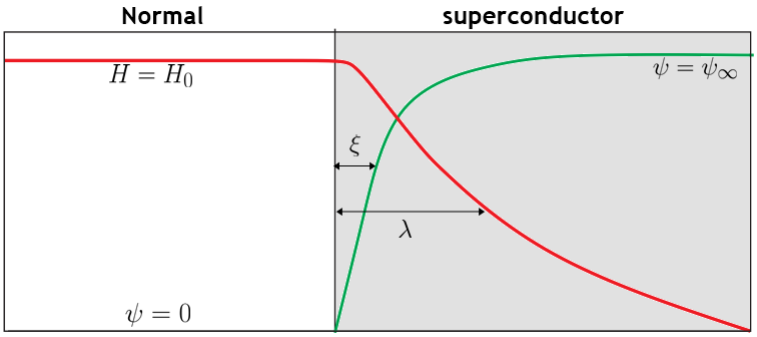

Figure 2.2: characteristic lengths for the field (red) and order parameter (green) variations in a normal-superconductor interface.

it as the **penetration depth**, which in analogy to the London theory we will represent by the Greek letter λ (Fig.2.2).

Considering low temperatures and weak magnetic fields, such that $|\psi|^2$ is practically its value in the absence of fields, $|\psi_\infty|^2$, we can assume $\psi^*\nabla\psi - \psi\nabla\psi^* \simeq 0$ (note that this expression is valid for a constant phase,$\nabla\varphi = 0$), the second GL-equation is reduced to

$$\mathbf{j}_s = -\frac{e^{*2}|\psi|^2}{m^*}\mathbf{A}(x). \tag{2.16}$$

Using the Ampère's law $\mu_0\mathbf{j} = \nabla \times \mathbf{B}$, and applying the curl operator to both sides of the above expression, we easily obtain the London Equation, Eq. (2.2), where the penetration depth will be given by

$$\lambda^2 = \frac{m^*}{\mu_0 e^{*2}|\psi|^2} = \frac{m^*\beta}{\mu_0 e^{*2}|\alpha|} \simeq \frac{\lambda^2(0)}{1 - T/T_c}. \tag{2.17}$$

For $T = 0$, λ is reduced to the London penetration depth, $\lambda(0) = \lambda_L$, when all the electrons become superconductors and $|\psi|^2 = |\psi_\infty|^2 = n_s$ = const.

So, we also obtain that for $x \gg \xi$, when $\psi \simeq \psi_\infty$, the fields and currents basically follow the London solution, differing only near the normal-superconductor interface. For $0 < x \ll \xi$ we can expand $\psi(x)$ as $\psi(x) \simeq \psi_\infty \frac{x}{\sqrt{2}\xi} \Longrightarrow |\psi(x)|^2 = |\frac{\psi_\infty x}{\sqrt{2}\xi}|^2$. Looking back to Eqs. (2.16) and (2.17), λ is no longer constant and the fields and currents will suffer a correction near the surface, as illustrated in Fig.2.3. Note that, $x \longrightarrow 0$ implies that $B_z \longrightarrow B_0$ = const., and the current density vanishes.

Another parameter that can be defined here is the so-called Ginzburg-Landau parameter, $\kappa = \lambda(T)/\xi(T)$, which describes the relationship between the flux penetration in a

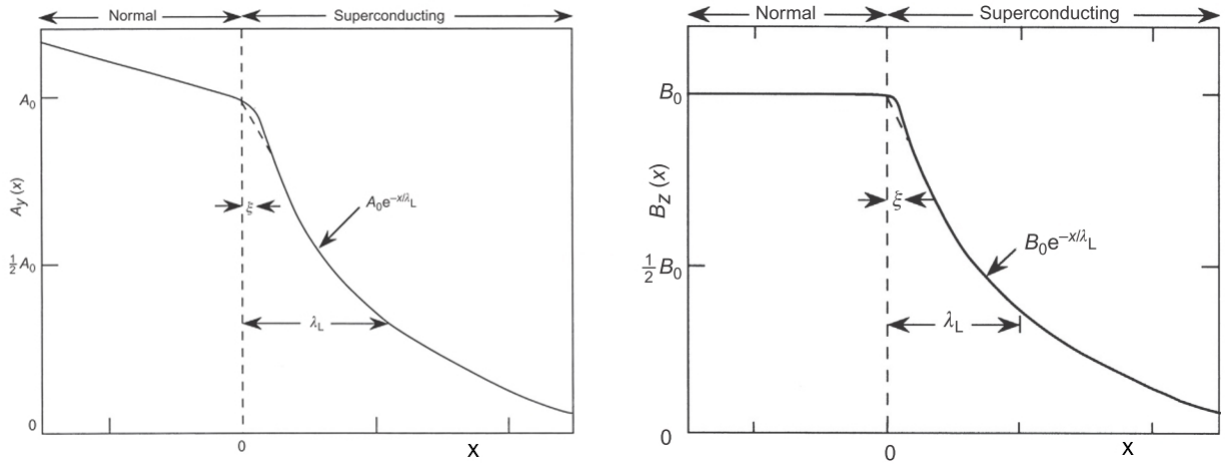

Figure 2.3: Fields and currents from the GL_theory for a normal-superconductor interface. Note that for $x \gg \xi$ it follows the London solution. (Figure taken from [11]).

superconducting material and the coherence of its superconductivity. Since λ and ξ have, in general, the same dependence on T, κ is a constant close to T_c.

The GL theory, although had been formulated for T near T_c, presents satisfactory results even when $T \ll T_c$. De Gennes [12], showed that the Ginzburg-Landau theory works for any temperature in strong magnetic fields.

2.4 Fluxoid quantization and the vortex state

Now we will proceed to investigate the situation when the sample is under an applied magnetic field. We saw before what happens with fields and currents near the surface when the superconductor is under a parallel applied magnetic field. Assume now that the magnetic flux penetrates deep inside the superconductor in an arbitrary region, S_0, far from the surface. We will see in this section that the magnetic flux crossing S_0 is quantized and vortices of currents will arise in order to preserve the superconductivity in the rest of the material.

2.4.1 *Fluxoid quantization*

Assume an arbitrary magnetic flux, Φ, crossing S_0. If we consider $\psi(\mathbf{r}) = |\psi(\mathbf{r})|e^{i\varphi(\mathbf{r})}$ in the second GL-equation, we obtain

$$\mathbf{j}_s = \frac{e^*\hbar}{m^*}|\psi|^2\nabla\varphi(\mathbf{r}) - \frac{e^{*2}}{m^*}|\psi|^2\mathbf{A}. \tag{2.18}$$

Then, taking the line integral around a closed contour Γ_0 surrounding S_0 (with Γ_0 far from S_0 and surfaces), the left side of the above expression goes to zero, since in the region between S_0 and the boundary there is no local magnetic fields or currents. Reorganizing the terms, it results in

$$\oint_{\Gamma_0} \mathbf{A}\cdot d\mathbf{l} = \frac{\hbar}{2e}\oint_{\Gamma_0} \nabla\varphi\cdot d\mathbf{l}, \tag{2.19}$$

where we used $e^* = 2e$. Once ψ is single-valued, the integral in the right must be equal to a multiple of 2π. On the other hand, the integral in the left gives us the magnetic flux inside the region surrounded by Γ_0. So we obtain the relation

$$\Phi = n\phi_0, \tag{2.20}$$

with $\phi_0 = h/2e$ the *quantum* of magnetic flux. Therefore, the magnetic flux crossing S_0 is quantized in multiples of $\phi_0 \simeq 2,07 \times 10^{-15} Tm^2$. This result was experimentally proven by *R. Doll et al* [13] and *B. S. Deaver et al* [14] in the same year, by independent research.

2.4.2 *Type I and type II superconductivity*

The presence of a critical field for superconductivity is a natural consequence of thermodynamics in the Gibbs formalism, where the destruction of the superconducting state is associated with the energy required to keep the field outside the material, $\mu_0 H^2/2$, where H is the applied field. When H reaches a critical field, H_c, the superconductivity is abruptly broken in a first order phase transition to the normal state. If we consider two superconducting states differing only by the applied magnetic field, zero for one and $H \neq 0$ for the other, the difference in the Gibbs free energy density between these two states will be given by $g_s(T,H) - g_s(T,0) = \mu_0 H^2/2$. Remember that, in the phase transition, the Gibbs free energy is continuous, i.e., $g_s(T,H_c) = g_n(T,H_c)$. Since the normal material has negligible magnetic susceptibility, the field contribution to the free

energy in normal state is negligible and $g_n(T, H_c) = g_n(T, 0)$. Rewriting the difference in energy for $H = H_c$ we obtain

$$\Delta g(T) = g_n(T, 0) - g_s(T, 0) = \frac{\mu_0 H_c^2}{2}. \tag{2.21}$$

Note that, $\Delta g(T)$ is the energy required to bring all electrons to the normal state, or, the condensation energy of the superconducting state at zero field. Empirically, H_c depends on temperature as

$$H_c(T) = H_c(0)\left(1 - \frac{T}{T_c}\right)^2, \tag{2.22}$$

as sketched in Fig.2.4.a.

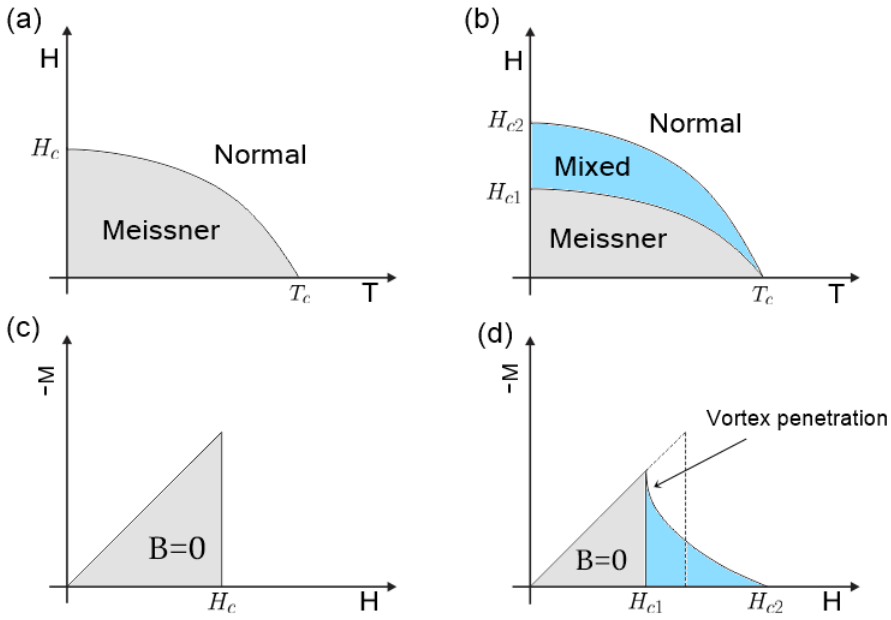

Figure 2.4: (a) Phase diagram for type-I superconductors, which presents only normal and Meissner states limited by $H_c(T)$.(b) Phase diagram for type-II. Here we can observe the vortex (mixed) state between the two critical fields $H_{c1}(T)$ and $H_{c2}(T)$. (c) Magnetization curve for type I superconductor, above H_c the magnetization goes to zero with the abruptly field penetration. (d) Magnetization curve for type-II. The partial flux penetration results in a smooth decay of the magnetization until reaching zero in $H = H_{c2}$.

This kind of superconductor that we described above is called "Type I superconductor". Until 1957 it was the only form of superconductivity theoretically studied, when Alexei Abrikosov [15] investigated the behavior of superconductors with the coherence length

smaller than the penetration depth in the presence of magnetic field. In this case, the penetration of magnetic flux below H_c is energetically favourable, since the surface energy becomes negative for $\xi < \lambda$. According to Abrikosov, this flux would be broken in as many parts as possible in order to minimize energy, the ground state would be the one in which each part would have exactly one quantum of magnetic flux, being therefore indivisible. Thus, along the flux lines, the superconductivity will be locally broken, and consequently, circular shield currents, or **vortices** of currents, will emerge around those regions in order to isolate the affected areas and preserve the superconductivity in the rest of the material. In this situation, the superconductor is said to be in the mixed state, and the superconductivity is called type II, which is characterized by two critical fields, H_{c1} and H_{c2}.

The lower critical field, H_{c1}, is related to the energy needed to nucleate a single vortex inside superconductor. That is, below H_{c1} the superconductor is still in Meissner state (zero magnetic flux inside it). Then, above this field value and below H_{c2}, vortices will penetrate, i.e., the mixed state appears until $H = H_{c2}$ when the material is completely filled by the flux lines and finally becomes in normal state (Fig.2.4.b). H_{c1} can be expressed by the following relation

$$H_{c1}(T) = \epsilon_v(T)/\phi_0, \tag{2.23}$$

where $\epsilon_v(T)$ is the vortex-line energy. In the next topic we will see that, for $\kappa \gg 1$, ϵ_v depends on temperature as $\lambda^{-2}(T) \sim (1 - T/T_c)^2$.

The upper critical field, H_{c2}, can be calculated from the first GL-equation, considering an infinite sample under an uniform magnetic field. If $H \longrightarrow H_{c2}$, $|\psi|$ becomes small and we can rewrite Eq.(11) in its linearized form, despising the term $\beta|\psi|^2$. In that way, the problem is reduced to solve a Schrodinger-like equation for a free particle of mass m^* and charge $e^* = 2e$, under an uniform magnetic field H, where, from the eigenvalues of energy, we obtain that the magnetic field H has a maximum possible value given by

$$H_{c2}(T) = \frac{\phi_0}{2\pi\mu_0\xi^2(T)} = \sqrt{2}\kappa H_c(T). \tag{2.24}$$

Note that, $\kappa < 1/\sqrt{2}$ implies in a upper critical field less than H_c. In this case the mixed state does not make sense, since in that field value the system do not have the energy required to bring all electrons to the normal state, which is only reached in $H = H_c$. Therefore, in this case the superconductor will be of type-I. For $\kappa > 1/\sqrt{2}$ the mixed state

becomes possible and the superconductivity is of type-II. Fig.2.4.(c) and (d) illustrate the magnetization, $M = \frac{B}{\mu_0} - H$, for type I and II, respectively. Observe that, in the Meissner state $B = 0$, therefore $M = -H$ for both kinds of superconductivity. However, apart from surface effects, the magnetic flux abruptly penetrates type-I samples at $H = H_c$, making $B = \mu_0 H$, and consequently $M = 0$. For type-II materials, the penetration is gradual, and the density of magnetic flux increases smoothly as the vortices are accommodated inside the sample, resulting in a soft decay of the magnetization until reaching zero in $H = H_{c2}$.

2.4.3 *The vortex at the limit $\kappa \gg 1$*

Like a tunnel crossing a mountain, the Abrikosov vortex leads the flux line from one side to another of the superconductor, shielding it, since along the flux line the superconductivity is locally broken. Analogously to the normal-superconductor interface, the fields and currents will vary radially within a characteristic length λ, and the order parameter in a coherence length ξ, as sketched in Fig.2.5. We call **vortex core** the region of radius ξ around the flux line, where the order parameter varies quickly. We will see along this section that is energetically favourable for the vortex to assume a linear shape and carry a single magnetic flux quantum ϕ_0 , i.e., $n = 1$ in Eq. (2.20).

The vast majority of type-II superconductors have $\lambda \gg \xi$. Such property simplifies our calculations about superconducting vortices, since for small values of ξ, the order parameter is basically constant outside the vortex cores. Therefore, making $|\psi|^2 = |\psi_\infty|^2$ in Eq. (2.18), using Ampere's law , and taking the curl operator in both sides of the equation, we obtain the following expression to the local magnetic field

$$-\lambda^2 \nabla^2 \mathbf{b} + \mathbf{b} = \frac{\phi_0}{2\pi} \nabla \times \nabla \varphi. \tag{2.25}$$

This is basically the London equation plus a term due to the flux penetration. Then, if we consider a linear isolated vortex positioned at the origin of the xy plane and oriented in the z direction, in a bulk infinite superconducting sample, the integral of the right side of the Eq.(2.25) will give us the magnetic flux of the vortex. Note that, the integral of $\nabla \times \nabla \varphi$ on the area, by Stokes theorem, becomes the line integral in the right-hand side of Eq. (2.19). As mentioned before, it must be equal to $2\pi n$, with n an integer number. Therefore, the right side of Eq.(2.25) can be rewritten in terms of a Dirac delta function, $\nabla \times \nabla \varphi = 2\pi n \delta(\mathbf{r})\hat{z}$, where $\mathbf{r} = 0$ is the vortex position. The parameter $n\delta(\mathbf{r})\hat{z}$

is know as the *vorticity* of the vortex, $\boldsymbol{\nu}(\mathbf{r})$, that represent the direction, position and the number of magnetic quanta carried by the vortex. Now, Eq.(2.25) can be easily solved by Fourier transform. Using $\mathbf{b}(\mathbf{r}) = b(\mathbf{r})\hat{z}$, we have

$$-\lambda^2(-iq)^2 b(\mathbf{q}) + b(\mathbf{q}) = n\phi_0, \tag{2.26}$$

and

$$b(\mathbf{q}) = \frac{n\phi_0}{\lambda^2 q^2 + 1}. \tag{2.27}$$

Taking the inverse transform, we obtain

$$b(r) = \frac{n\phi_0}{2\pi\lambda^2} K_0\left(\frac{r}{\lambda}\right), \tag{2.28}$$

where K_0 is the zeroth-order modified Bessel function of the second kind. This function has asymptotic behaviour given by

$$K_0\left(\frac{r}{\lambda}\right) \approx \ln\left(\frac{1.123\lambda}{r}\right) \quad , \quad r \ll \lambda \tag{2.29}$$

$$K_0\left(\frac{r}{\lambda}\right) \approx \frac{\exp(-r/\lambda)}{(2r/\pi\lambda)^{\frac{1}{2}}} \quad , \quad r \gg \lambda. \tag{2.30}$$

Note that $b(r)$ diverges for $r \longrightarrow 0$. This divergence occurs because we did not consider the vortex core and it is usually solved by taking a cutoff in $r \sim \xi$. To preserve the continuity of $b(r)$ and avoid the divergence near the vortex core, J.R. Clem [16], proposed the following correction in the radial coordinate, $r \longrightarrow \sqrt{r^2 + 2\tilde{\xi}^2}$. This is a good approximation valid for $\kappa \gg 1$. Fig.2.5 illustrates $b(r)$ and $|\psi(r)|^2$ for an isolated vortex.

The free energy density of a superconductor with an isolated vortex inside can be written as (see Eq. (2.9))

$$f_s = f_M + \frac{1}{2}mv_s^2|\psi|^2 + \frac{b^2}{2\mu_0}, \tag{2.31}$$

where f_M is the free energy density in the Meissner state and v_s is the modulus of the superfluid velocity. $\mathbf{v}_s$ is related to the momentum operator by $\mathbf{P} = -i\hbar\nabla - e^*\mathbf{A}(\mathbf{r}) = m^*\mathbf{v}_s$, where, substituting this relation in the second GL equation, we obtain that $\mathbf{v}_s = \mathbf{j}_s/2e|\psi|^2$. Looking back at Eq.(2.31), the energy cost of a vortex will be given by

$$E_v = \int d\mathbf{r}(f_s - f_M). \tag{2.32}$$

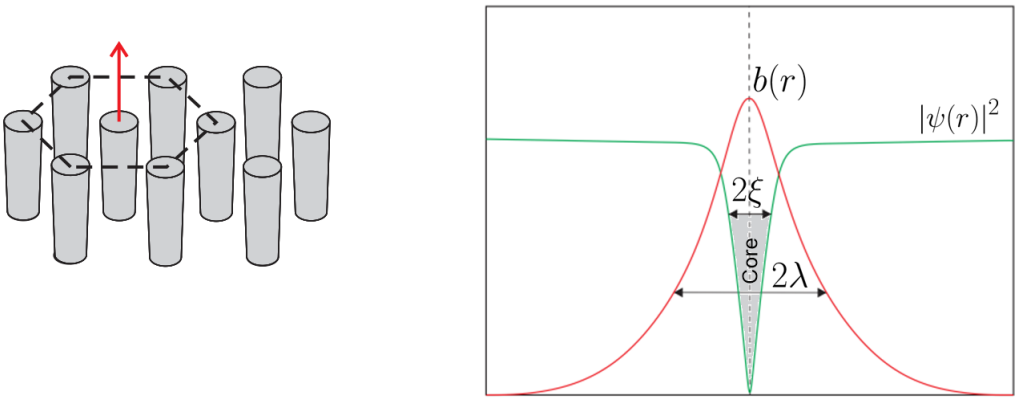

Figure 2.5: Left: Hexagonal arrangement for linear vortices in an Abrikosov lattice. Right: Isolated vortex structure, showing the spatial variations of the induced magnetic field and order parameter. Note that we used the Clem approximation $r \longrightarrow \sqrt{r^2 + 2\xi^2}$ in order to avoid the divergence of $b(r)$ near the vortex core.

Substituting v_s in Eq.(2.31) and considering de region $r > \xi$, i.e.,$|\psi| = |\psi_\infty|$, Eq.(2.32) becomes

$$E_v = \frac{1}{2\mu_0} \int_{r>\xi} d\mathbf{r}[\lambda^2(\nabla \times \mathbf{b})^2 + \mathbf{b}^2]. \tag{2.33}$$

Using the identity $\nabla \cdot (\mathbf{a} \times \mathbf{b}) = \mathbf{b} \cdot (\nabla \times \mathbf{a}) - \mathbf{a} \cdot (\nabla \times \mathbf{b})$, with $\mathbf{a} = \nabla \times \mathbf{b}$, Eq.(2.33) can be rewritten as

$$E_v = \frac{1}{2\mu_0} \int_{r>\xi} d\mathbf{r}(\mathbf{b} \cdot [-\lambda^2 \nabla^2 \mathbf{b} + \mathbf{b}]) + \frac{\lambda^2}{2\mu_0} \int d\mathbf{r} \nabla \cdot [\mathbf{b} \times \nabla \times \mathbf{b}]. \tag{2.34}$$

As we know, $-\lambda^2 \nabla^2 \mathbf{b} + \mathbf{b} = \phi_0 n \delta(\mathbf{r})$, therefore the first integral vanishes for $r > \xi$. The second integral can be transformed in a surface integral by the divergence theorem, to be performed in the surfaces $r = \xi$ and $r = \infty$. The contribution of the second integral is negligible since $\mathbf{b}$ goes to zero when $r \longrightarrow \infty$. Using the asymptotic approximation (Eq. (2.29)) the integral results in

$$\epsilon_v = \frac{E_v}{L} = n^2 \frac{\phi_0^2}{4\pi\mu_0\lambda^2} \ln \kappa = n^2 \epsilon_0 \ln \kappa, \tag{2.35}$$

where L is the length of the vortex. Note that the energy of the vortex is proportional to its length and to n^2. Therefore, it is energetically favourable for the vortex to assume a linear shape along the same direction of the applied field, and with magnetic flux ϕ_0

,i.e., $n = 1$ in Eq.(2.22). We will see in the next topic that this is true even considering the interaction energy between the vortices.

2.4.4 *Vortex-vortex interaction*

Consider now two linear vortices oriented in the z direction and positioned in $\mathbf{r}_1$ and $\mathbf{r}_2$ on the xy plane. Each vortex interact with the other through their current distributions. The vortex 1 suffers a Lorentz force per unit of length, $\mathbf{f}_{12}$, due to the currents of the vortex 2, $\mathbf{j}_2$, given by

$$\mathbf{f}_{12} = \mathbf{j}_2(r_{12}) \times (\phi_0 \hat{z}), \tag{2.36}$$

where $r_{12} = |\mathbf{r}_1 - \mathbf{r}_2|$ is the distance between the vortices. We know that $\mu_0 \mathbf{j} = \nabla \times \mathbf{b}$, and using Eq.(2.28) for $\mathbf{b}$ in z direction, we obtain

$$\mathbf{f}_{12} = -\frac{\phi_0^2}{2\pi\mu_0\lambda^2}\frac{\partial K_0(r_{12}/\lambda)}{\partial r_{12}} = \frac{\phi_0^2}{2\pi\mu_0\lambda^3}K_1(r_{12}/\lambda), \tag{2.37}$$

where K_1 is the first-order modified Bessel function. The energy per unit length, similar to the isolated vortex, can be calculated from Eq.(2.33), but now $\mathbf{b}(\mathbf{r}) = \mathbf{b}_1(\mathbf{r}) + \mathbf{b}_2(\mathbf{r})$ and the surface integral will be taken avoiding the two cores. The resulting energy for the two-vortex system is

$$\epsilon_{2v} = 2\epsilon_v + 2\epsilon_0 K_0(r_{12}/\lambda), \tag{2.38}$$

where the second term on the right side gives us the interaction energy. At the limit $r_{12} = \xi$, using Eq. (2.29), we have $K_0(\xi/\lambda) \simeq \ln\kappa$, and the above expression becomes $\epsilon_{2v} \simeq 4\epsilon_0 \ln\kappa$. If we consider a vortex with two quanta of magnetic flux, i.e., $n = 2$ in Eq. (2.35), we obtain $\epsilon_v^{n=2} = 4\epsilon_0 \ln\kappa$. Therefore, since at $r_{12} = \xi$ the interaction term has the maximum value, $\epsilon_{2v} \leq \epsilon_v^{n=2}$. Consequently, for $H \ll H_{c2}$, when the vortices are separated by distances greater than ξ, the ground state is the one in which each vortex has one quantum of magnetic flux.

The repulsive force between the flux lines results in a periodic solution for the positions of the vortices in an homogeneous superconductor, i.e., the ground state is a periodic vortex-lattice, where the hexagonal lattice (or Abrikosov lattice) presents the lowest energy (Fig. 2.5).

2.4.5 *Thin films*

Consider a superconducting film of thickness $d \ll \lambda$ under a **perpendicular** applied magnetic field. In this case, local fields and currents are practically constant along the thickness and the vortices are basically punctual in the London approximation. In this case, it is convenient to treat this problem using the vector potential, $\mathbf{A}$, rather than the magnetic field. Similarly to the bulk sample we start from Eq.(2.25), rewriting it in terms of $\mathbf{A}$,

$$\nabla \times (\mathbf{A} + \mu_0 \lambda^2 \mathbf{j}_s) = \phi_0 \delta(\mathbf{r}) \hat{z}, \tag{2.39}$$

where we can define $\Phi \equiv \mathbf{A} + \mu_0 \lambda^2 \mathbf{j}_s$ with the condition $\nabla \times \Phi = \phi_0 \delta(\mathbf{r}) \hat{z}$. Using that $\nabla \times (\hat{\theta}/r) = 2\pi\delta(\mathbf{r})\hat{z}$, we have $\Phi = (\phi_0/2\pi r)\hat{\theta}$. Now, taking the average over the thickness d, we define the sheet current $\mathbf{J} = \int \mathbf{j}_s dz = \mathbf{j}_s d$. Organizing the terms it results in

$$\mathbf{J} = \frac{1}{\mu_0 \lambda_{eff}} (\Phi - \mathbf{A}) \qquad \text{for} \quad |z| \leq \frac{d}{2}, \tag{2.40}$$

where $\lambda_{eff} = \lambda^2/d$ is the effective penetration depth of the film. If we assume a sheet current flowing only in the $z = 0$ plane, i.e., $\delta(z)\mathbf{J}$. Then we rewrite Eq.(2.40) as

$$-\nabla^2 \mathbf{A} + \frac{\delta(z)\mathbf{A}}{\lambda_{eff}} = \frac{\delta(z)\Phi}{\lambda_{eff}} \tag{2.41}$$

Note that we used the relation $\nabla \times \nabla \times \mathbf{A} = -\nabla^2 \mathbf{A} = \mu_0 \mathbf{J}$, in the London gauge. Eq.(2.41) can be solved by the Fourier transform method (De Gennes [17]), and has the solution in the Fourier space given by

$$\mathbf{J}_q = \frac{1}{\lambda_{eff}} \left(\Phi_q - \frac{\Phi_q}{1 + 2q\lambda_{eff}} \right), \tag{2.42}$$

where Φ_q is the Fourier transform of Φ. The interaction energy between two vortices will be determined by the Lorentz force $\mathbf{F}(r) = \mathbf{J}(r) \times (\phi_0 \hat{z})$. Substituting $\mathbf{J}$ and using that in the Fourier space $\mathbf{F}(\mathbf{q}) = -i\mathbf{q}E_{vv}(\mathbf{q})$, we obtain

$$E_{vv}(\mathbf{q}) = \frac{\phi_0^2}{q\mu_0} \frac{1}{1 + 2q\lambda_{eff}}. \tag{2.43}$$

At small distances, $r \ll \lambda_{eff}$, or $\mathbf{q} \gg \lambda_{eff}^{-1}$, Eq.(2.43) is reduced to $E_{vv}(\mathbf{q}) = \phi_0^2/2q^2\mu_0\lambda_{eff}$, returning to the original space

$$E_{vv}(r) = \frac{\phi_0^2}{2\pi\mu_0\lambda_{eff}} \ln\left(\frac{\lambda_{eff}}{r}\right). \tag{2.44}$$

The self energy of the vortex can be calculated similarly to the bulk sample (Eq. (2.35)), just replacing λ by λ_{eff}.

2.4.6 Vortex motion

The dynamics of the flux lines within the superconductor will be governed by the forces acting on the system. For a vortex in a homogeneous superconductors , the movement will be determined by the Lorentz force $\mathbf{F}_L = \mathbf{j} \times (\phi_0\hat{z})$, where $\mathbf{j}$ can come from any current source. The Lorentz force pushes the flux line through the material. During this movement, a viscous force opposing the motion arises. Such force is due to the scattering processes suffered by the normal electrons inside the vortex core. In this case, the vortex moves with terminal velocity (overdamped motion) determined by the coefficient η, i.e., $\mathbf{F}_L = \eta\mathbf{v}$, where $\mathbf{v}$ is the terminal velocity of the motion. Thus, the equation of motion for the vortex is given by

$$\eta\mathbf{v} = \phi_0\mathbf{j} \times \hat{z}. \tag{2.45}$$

This regime in which the vortices are in linear motion is called *flux flow*. Note that, when the magnetic flux ϕ_0 starts to move, an electric field appear, which follows from the relation $\mathbf{E} = \frac{\phi_0\hat{z}}{A} \times \mathbf{v}$, where A is the area of the vortex core in xy plane. In this way an electrical resistance is also associated to the movement, with resistivity ρ_{ff} (flux flow resistivity) given by $\mathbf{E} = \rho_{ff}\mathbf{j}$. Substituting $\mathbf{v}$ in terms of $\mathbf{E}$ in Eq.(2.45) we can write $\rho_{ff} = B\phi_0/\eta$. Thus, the superconductor loses one of its main characteristics when the vortex motion occurs: the null electrical resistivity. In 1965, Bardeen and Stephen [18] assumed that the dissipation results from a purely resistive process inside the vortex core and found that, in this case, $\eta = \phi_0 B_{c2}/\rho_n$, where ρ_n is the resistivity in the normal state extrapolated for the specific temperature.

The above situation refers to a homogeneous superconductor. However, most superconductors present structural defects that act as pinning centers for vortices. Such inhomogeneities can be taken into account by an effective pinning potential, U_p, rep-

resenting the interaction between vortices and the pinning centers. Thus, if we also consider a thermal shaking, we obtain the Langevin equation

$$\eta \mathbf{v} = \phi_0 \mathbf{j} \times \hat{z} - \nabla U_p + \Gamma(T, t), \tag{2.46}$$

where $\Gamma(T, t)$ is the stochastic Langevin force representing the effect of the collisions with the atoms of the superconducting crystal at a temperature T, as in the Brownian motion of microscopic particles diluted in a fluid. The regime in which the vortices are initially pinned but, due to a small applied current and the thermal shaking, can detach from a pinning site to another, is called *flux creep*. In this situation, the resistivity ρ_{fc} is less than ρ_{ff}, since the dissipated energy is related to the velocity of the vortices. In the situation where the thermal fluctuations are negligible, the vortex motion only occurs when $\mathbf{j}$ produces a force greater than the pinning force.

Eq.(2.46) can be used in several situations even for different kinds of particles, but we have to pay attention to satisfy some conditions before using it. For example, the dynamics needs to be overdamped; the temperature must be homogeneous, or a well-know $T(\mathbf{r})$; the vortex cores must be able to be treated as punctual, in order to follow the Brownian motion; and the vortex can not move so fast, otherwise there would not be enough time for the cooper pairs to recombine after the vortex passage; these among other precautions.

2.5 Flux penetration in inhomogeneous superconductors

In the previous section we saw that inhomogeneities in the material can imprison the vortices, which can move in a flux creep motion under a low applied current. Consider now a slab superconducting sample with a strong pinning potential, which may be either naturally or artificially produced [19]. In this case the vortex will move only if the local current reaches a critical value, $\mathbf{j}_c$, where the Lorentz force becomes greater than the pinning forces. It is convenient now to look at the whole system macroscopically, since each vortex have a particular, irregular, motion determined by the local pinnnig sites. Thus, we must observe the flux moving in bundles, where the driving force per unit volume exceeds the pinning forces available in the same volume.

2.5.1 *Critical state*

Imagine the sample is submitted to a parallel applied magnetic field. As we saw before, the vortices will penetrate through the vacuum-superconductor interface for $H > H_{c1}$, but note that they will accumulate in the pinning sites. Therefore, we must expect a high density of vortices near the surface which decays toward the center of the sample. If the local current density j (which depends on the Meissner and vortices current) is higher than j_c, the vortices keep moving through the sample until they find a comfortable position, where $j < j_c$.

The Bean model [20], assumes that regardless of the applied magnetic field , at the equilibrium, the current density in the vortex gradient region is constant and equal to j_c, i.e., $b(x)$ has constant inclination. Fig.2.6. shows $b(x)$ for different values of applied field, increasing and decreasing it. When the field is decreased the vortices near the surface leave the sample, thus forming a gradient with the opposite sign of the penetration case.

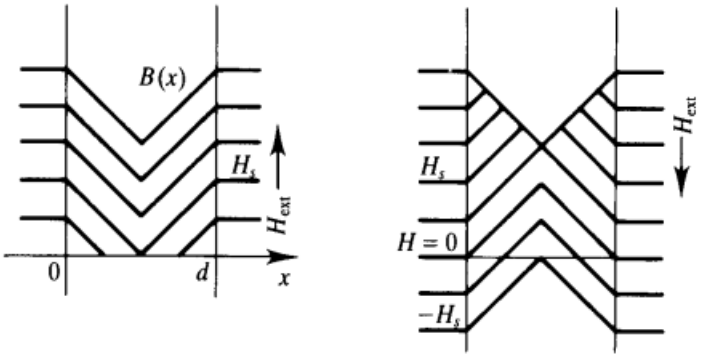

Figure 2.6: Magnetic field profiles for the Bean Model, increasing (left) and decreasing (right) the external applied field. The critical current is considered constant in all the vortex gradient region. (This figure was taken from [21]).

Note that in the decreasing-field process there is always magnetic flux inside the superconductor, even for $H = 0$. This occurs because some vortices are still pinned in the inhomogeneities of the material. Thus, the magnetization assumes different values for the same applied field **H**, depending on the magnetic history of the system, resulting in a hysteresis loop.

The Bean model is the simplest and the most used among the critical state models that have been proposed to describe the flux penetration in an inhomogeneous superconductor. But, even though it can satisfactorily describe the low-field cases with several

experimental confirmations, it starts to fail when the magnetic field grows enough to reach the center of the sample. Each critical state model is based on a particular assumed relationship between the internal field and the critical current density. Table 2.1 presents the most used critical-state models. All of them depends on the parameters B_k and J_k associated with the internal field and current density.

Equation	Model
$j(b) = j_c$	Bean [22]
$j(b) = \frac{J_k}{\lvert b(x)\rvert / B_k}$	Fixed pinning [23]
$j(b) = \frac{J_k}{\lvert b(x)/B_k\rvert^{1/2}}$	Square root [23]
$j(b) = \frac{J_k}{1+\lvert b(x)\rvert / B_k}$	Kim [24]
$j(b) = J_c \exp(-\lvert b(x)\rvert / B_k)$	Exponential [25]
$j(b) = \frac{J_k}{1+[\lvert b(x)\rvert / B_k]^2}$	Quadratic [11]

Table 2.1: The most used critical-state models. Observe that the Kim, Quadratic and Exponential models are reduced to the Bean model when $\lvert b(x)\rvert \ll B_k$.

Fig.2.7 illustrates the typical high-field magnetization loops for zero and strong pinning potentials. Shimizu and Ito (1989) [26], proposed an indirect method of measuring J_c using hysteresis loops, where they found that the critical current is proportional to the width of the magnetization hysteresis curve, ΔM. Thus, looking at Fig.2.7, we also expect J_c to depend on the magnetic field.

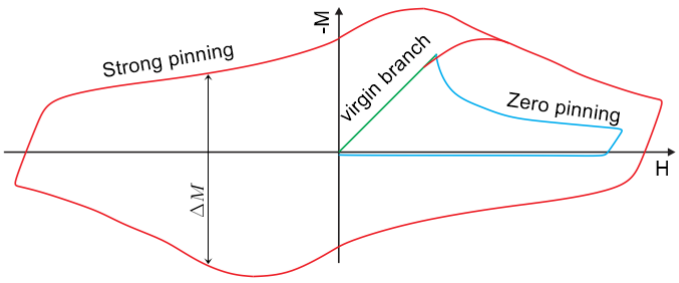

Figure 2.7: Typical high-field magnetization loop for zero (cyan) and strong (red) pinning potentials. The green line represents the so-called "virgin branch", when there is no flux penetration yet and the superconductor is still in the Meissner state.

2.6 Vortex lattice as a 2D crystal

Due to their repulsive interactions, the vortices tend to form a regular lattice which can be compared to several interacting particle systems. Even the vortex having the geometry of a line, on the xy-plane it can be approximately seen as a point-like particle, where we have to pay attention on the elasticity of the lattice before assume this approximation. The three-dimensional vortex lattice has basically three elastic modes: *compression*, *shear* and *tilt* [19, 27]. For thin films, where the length of the vortex is negligible, and for perfectly linear vortices, the elastic modes are reduced to those of a two-dimensional crystal: *compression* and *shear*. Fig.2.8 presents an artistic representation of the graphene as a 2D crystal [28], and a scanning tunnel microscopy (STM) image of the vortex lattice in a sample of $NbSe_2$ [29].

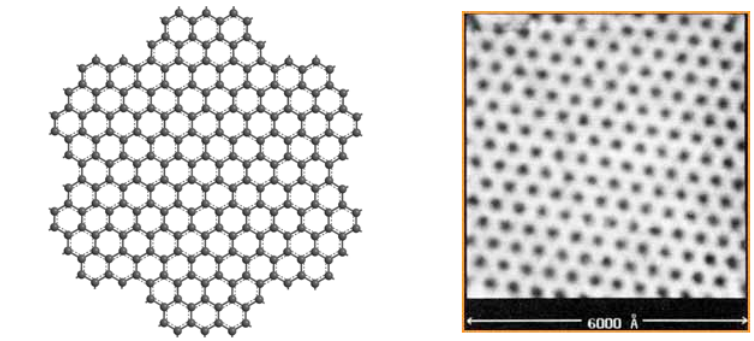

Figure 2.8: a) Artistic representation of the graphene structure (figure taken from [28]). Note that if we imagine a particle positioned inside each graphene cells we obtain the hexagonal lattice. b) STM image of a vortex lattice in NbSe2, 1989 (figure taken from [29]).

2.6.1 *Vortex lattice melting*

If we increase sufficiently the thermal shaking, the Abrikosov lattice will lose the positional and topological order, becoming the so-called liquid of vortices. In this phase, the shear elastic-mode is null and the system forms a kind of vortex-soup. Although the melting of the vortex lattice has been studied for some decades, a complete theory of this transition has not been formulated yet. Some works about this theme can be found in [30–34]. Fig.2.9 presents the scanning tunnelling spectroscopy (STS) images of

the vortex lattice, before and after melting in a W-based superconducting thin film [35]. The phase diagram for a homogeneous superconductor is sketched in Fig.2.9.c.

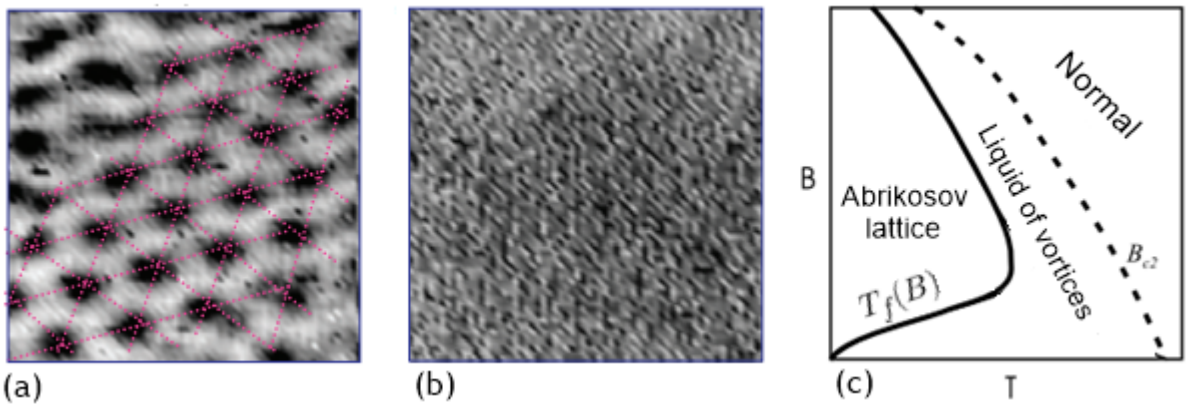

Figure 2.9: (a) Vortex lattice at 1.2 K, before melting (b) the same system at 3.0 K, no isolated vortices are seen, the vortex lattice formed an isotropic liquid.(figures taken from [35]). (c) Phase diagram for the vortex lattice for a homogeneous superconductor. The solid line indicates an abrupt first order phase transition, while the dashed line indicates a continuous transition.

To estimate the melting temperature we can rely on Lindemann's criterion [36], which assumes that the melting is expected when the vibration root mean square amplitude of the particles, $\sqrt{\langle u^2 \rangle}$, exceeds a threshold value proportional to the typical distance between the particles, a (e.g.,for a hexagonal lattice a is the edge of the hexagon). In other words, the melting temperature will be given by

$$\langle u^2(T_f) \rangle = c_L^2 a^2, \tag{2.47}$$

where, c_L is a constant of empiric value $c_L \sim 0.1 - 0.2$. Even though elasticity theory fails in describing the nature of the phase transition, since it loses its validity near the transition, it can be used to calculate $\langle u^2 \rangle$. Frey, Nelson and Fisher (1994) [37], proposed an elastic model, known as *cage* model, that simplifies the calculation of the vibration root mean square. They assumed a central vortex that can be deformed, i.e., $\mathbf{u} \neq 0$, surrounded by linear vortices that do not suffer distortions and produce a cage-potential on the central vortex. In this way they could find the relation $\langle u^2 \rangle \approx k_B T / \sqrt{\kappa \epsilon_v}$. Returning to the Lindemann's criterion we obtain

$$k_B T_f \approx c_L^2 \sqrt{\epsilon_v \kappa} a^2. \tag{2.48}$$

From Frey et al [37], $\kappa \simeq [\partial^2 E_{vv}/\partial r^2]_{r=a}$. In the cases $\lambda \gg a$ and $\lambda \ll a$, the interaction energy becomes $E_{vv} = -\epsilon_0 \ln(r/\lambda)$ and $E_{vv} = \epsilon_0 \sqrt{\pi\lambda/2r}\exp(-r/\lambda)$ respectively, and Eq.2.48 assumes the asymptotic expressions

$$k_B T_f \approx c_L^2 \epsilon_0 a = c_L^2 \sqrt{\frac{2}{3}} \frac{\phi_0^{-\frac{1}{2}}}{4\pi\mu_0\lambda^2} B^{-\frac{1}{2}} \quad , \quad \lambda \gg a, \tag{2.49}$$

$$k_B T_f \approx c_L^2 \epsilon_0 a \left(\frac{a}{\lambda}\right)^{\frac{3}{4}} e^{-a/\lambda} \quad , \quad \lambda \ll a, \tag{2.50}$$

where we used $B = n\phi_0$ with $n = 2/\sqrt{3}a^2$ for the hexagonal lattice. For low field values, $B \gtrsim \mu_0 H_{c1}$, the vortices interact weakly and are separated by $a \gtrsim \lambda$. In this case $T_f(B)$ is given by Eq.(2.50). For intermediary field values, $\mu_0 H_{c1} \ll B \ll \mu_0 H_{c2}$, the vortices are closer ($\xi \ll a \ll \lambda$) and $T_f(B)$ is given by Eq.(2.49). Fig. 2.9 shows $T_f(B)$ in the phase diagram for the vortex lattice for a homogeneous superconductor.

3 Vortex Dynamics and Surface Effects in the Critical State

In the previous chapter we studied the structure of isolated vortices deep inside the superconductor and how they form an hexagonal lattice. But, what happens when the vortex is near the surface? In this chapter we analyse the surface effects on the vortex dynamics and configurations. We perform numerical simulations for the vortex penetration and analyse the nonuniform distributions of the critical state and how it can be changed by the pinning potential and surface effects. In what follows we assume the London approximation ($\kappa \gg 1$).

3.1 Entry barriers

3.1.1 Bean-Livingston surface barrier

At first, let us consider a linear vortex in an infinite superconducting sample. As described in the previous chapter, the shielding currents encircling a straight vortex line deep inside a bulk superconductor flows symmetrically in circular paths. In contrast, when the vortex is near the vacuum-superconductor interface, the shielding currents will be deformed to satisfy the boundary conditions, which imposes that the current does not have normal components on the surface, since it can not pass through the boundary(see Fig. 3.1). This deformation results in a force pulling the vortex out of the sample, which can be compared to the Magnus force in hydrodynamics [38], where the difference in fluid velocities (in our case a quantum fluid of cooper-pairs) produce a resultant force on the object.

To solve this problem, i.e., find the currents and fields distributions, we can make use of the method of images (*Jackson, 1999* [39]), where in analogy to a point charge located near an infinite grounded conducting plane, we can imagine an antivortex

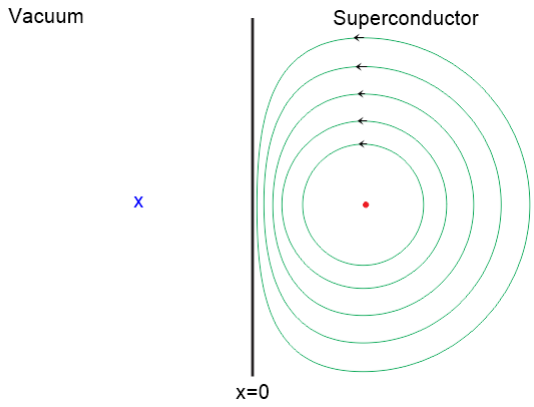

Figure 3.1: Vortex near the surface. The currents are deformed in order to satisfy the boundary conditions. To simulate this deformation we can assume an antivortex, symmetrically distanced from the surface, as a mirror reflect of the original vortex in the other side of the interface. The dot (red) represents the vortex core position and the x (blue) represents the antivortex core position

symmetrically distanced from the surface as a mirror reflection of the original vortex, in the other side of the interface (Fig. 3.1). The current of the antivortex rotates in an opposite direction in order to cancel the vortex current at the surface. In this case, and considering $x > 0$ the superconductor and $x < 0$ the vacuum region, where the vortex is positioned in (x_v, y_v) and the antivortex in $(-x_v, y_v)$, we obtain that the field distribution due to the vortex is given by

$$b_v(\mathbf{r}, \mathbf{r}_v) = \frac{\phi_0}{2\pi\lambda^2}\left[K_0\left(\frac{\sqrt{(x-x_v)^2+(y-y_v)^2}}{\lambda}\right) - K_0\left(\frac{\sqrt{(x+x_v)^2+(y-y_v)^2}}{\lambda}\right)\right] \quad , x > 0. \tag{3.1}$$

Note that the magnetic flux, Φ, carried by the vortex is also reduced depending on its distance from the surface. This flux can be calculated by integrating Eq.(3.1). With the help of the Fourier method, one can easily obtain $\Phi(x_v) = \phi_0(1 - e^{-x_v/\lambda})$, where for $x_v \gg \lambda$ we have $\Phi = \phi_0$. Naturally, we must expect a reduction in the self energy of the vortex when $x_v \longrightarrow 0$. The self energy as a function of x_v can be written as

$$\epsilon_v(r_v) = \frac{1}{2\mu_0}\phi_0 b_v(\mathbf{r}, \mathbf{r}_v)|_{r=r_v}, \tag{3.2}$$

where $b(\mathbf{r}, \mathbf{r}_v)$ is calculated in the vortex position and we consider the Clem approximation $r \longrightarrow \sqrt{r^2 + 2\xi^2}$ when the argument of K_0 goes to zero, in order to avoid

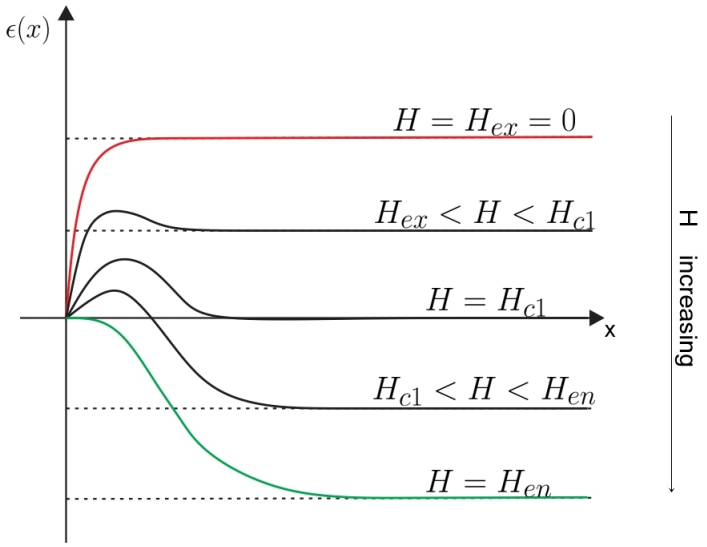

Figure 3.2: Bean-Livingston surface barrier. Due to the surface interaction the vortex can not penetrate before $H = H_{en}$, where H_{en} is a entry field value. Also observe that the vortices inside the superconductor cant go out for $H > H_{ex}$, even the minimum of energy being out side of the sample, where H_{ex} is the exit field.

the divergence in the vortex core (Fig 2.5). This method is equivalent to integrating Eq. (2.33). In this way, Eq.(3.2) can be rewritten as

$$\epsilon_v(x_v) = -\epsilon_0 \left[K_0\left(\frac{2x_v}{\lambda}\right) - K_0\left(\frac{\sqrt{2}\xi}{\lambda}\right) \right], \tag{3.3}$$

with $\epsilon_0 = \phi_0^2/4\pi\mu_0\lambda^2$. Note that for $x_v \gg \lambda$ the first term in the right side of the above equation goes to zero and , using the asymptotic approximation (Eq. (2.29)), Eq.(3.3) results in the self energy of an isolated vortex $\epsilon_v = \epsilon_0 \ln\kappa$. Since the self-energy depends on the vortex position, the interaction with the surface results in a force given by

$$\mathbf{f}_{self}(x_v) = -\frac{\partial\epsilon_v(x_v)}{\partial x_v}\hat{x} = -\frac{\phi_0^2}{2\pi\mu_0\lambda^3} K_1\left(\frac{2x_v}{\lambda}\right)\hat{x}, \tag{3.4}$$

which tends to pull the vortex out of the sample. Considering the interaction energy between the vortex and the Meissner field, $b_M(x_v)$, the total energy of the vortex becomes

$$\epsilon(x_v) = \epsilon_v(x_v) + \frac{\phi_0}{\mu_0} b_M(x_v) = -\epsilon_0 \left[K_0\left(\frac{2x_v}{\lambda}\right) - K_0\left(\frac{\sqrt{2}\xi}{\lambda}\right) \right] + \phi_0 H e^{-x_v/\lambda}, \tag{3.5}$$

where we used $b_M(x_v) = \mu_0 H e^{-x_v/\lambda}$ for a parallel applied field. Consequently, the resultant force acting on the vortex is

$$f_x(x_v) = -\frac{\phi_0^2}{2\pi\mu_0\lambda^3} K_1\left(\frac{2x_v}{\lambda}\right) + \frac{\phi_0}{\lambda} H e^{-x_v/\lambda}. \tag{3.6}$$

Observe that the Meissner force pushes the vortex into the sample while the self-force pulls it out. Thus, $f_x(x_v)$ can be positive or negative depending on which term is dominant. Now, imagine the situation in which the superconductor is initially in the Meissner state. Then, increasing the applied field we allow the vortex to nucleate at the surface. Note that, even though a minimum of energy is available deep inside the sample, the vortex needs to cross an energetic barrier created by the competition between the attractive energy, due to the interaction with the surface, and the repulsive energy of the Meissner field (Fig. 3.2). This energetic barrier is known as Bean-Livingston surface barrier [40].

Let us consider that the vortex is completely penetrated at a distance ξ from the surface. In this case the vortex remains into the sample only if $f_x(\xi) \geq 0$. In other words,

$$H \geq \frac{\phi_0}{2\pi\mu_0\lambda^2} K_1\left(\frac{2\xi}{\lambda}\right) e^{\xi/\lambda} \equiv H_{en}. \tag{3.7}$$

Here we defined the entry field H_{en}, at which the vortex can overcome the surface barrier. In non-homogeneous superconductors, as we will see during this chapter, the pinning sites can hold the vortices inside the material even for low applied fields, resulting in a entry field smaller than in the homogeneous case.

3.1.2 *Geometrical barrier*

For thin films under a perpendicular applied field another surface effect becomes relevant. Due to the high demagnetization effect, i.e., the field deformation that concentrate a high density of flux lines on the lateral surface (Fig. 3.3), the vortex penetration occurs first at the edges, where the field values are larger. Fig.3.3 illustrates the penetration process of a vortex in three different times, the chronological sequence is indicated by the colors. Starting by the edges (red lines), the flux line crosses the sample in two parts. The penetration keeps going until both parts touch each other (blue) and finally the vortex assumes the straight shape with energy $E = \epsilon_v d$ (green). Note that during the penetration the vortex assumes different lengths, with maximum

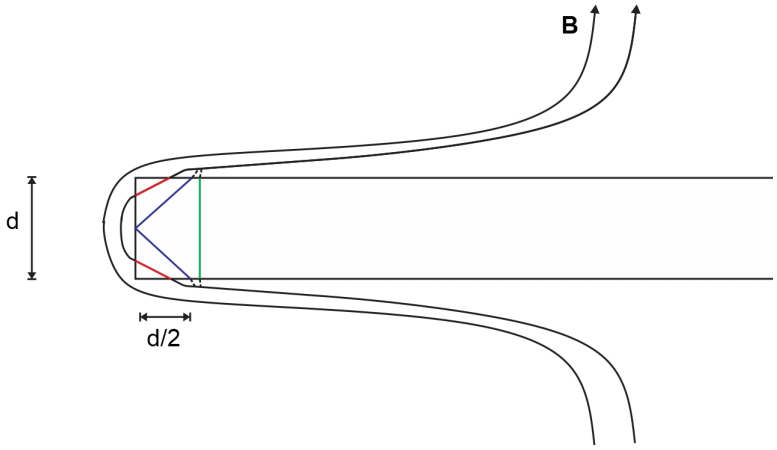

Figure 3.3: Geometrical barrier. The colors indicate different times of the penetration: Penetration begins (red); middle time (blue); penetration completed (green).

length approximately equals to $\sqrt{2}d$ (blue line). In that way, although the minimum of energy being inside the material, to penetrate, the vortex needs to assume an energy greater than $\epsilon_v\sqrt{2}d$. This energetic barrier is known as geometrical or edge barrier. Some other surface or edge barriers for the flux penetration into thin superconductors are discussed in Brandt,1995 [19]. However, in this chapter we are interested on the longitudinal geometry, where this kind of barrier is negligible due to the infinite longitudinal dimension.

3.2 Model and simulation details

In this section we give the details of the model and numerical methods used to simulate a vortex system in an inhomogeneous superconducting slab. We are interested here in analysing the surface effects on the vortex lattice and how it influences the critical state. For this, we model an infinite superconducting slab with thickness $D = 30\lambda$ (such that we can assume the approximation $D \gg \lambda$) under a parallel applied magnetic field (Fig 3.4.a). We consider that the vortices are rigid straight lines oriented parallel to the applied field, such that the energy of a vortex will be given by Eq. 3.5, where the surface effect is explicitly taken into account by the method of images. Thus, the problem can be reduced to calculating the two-dimensional dynamics of the vortex lines in the xy plane, in which case we can make use of the Langevin equation for the vortex motion.

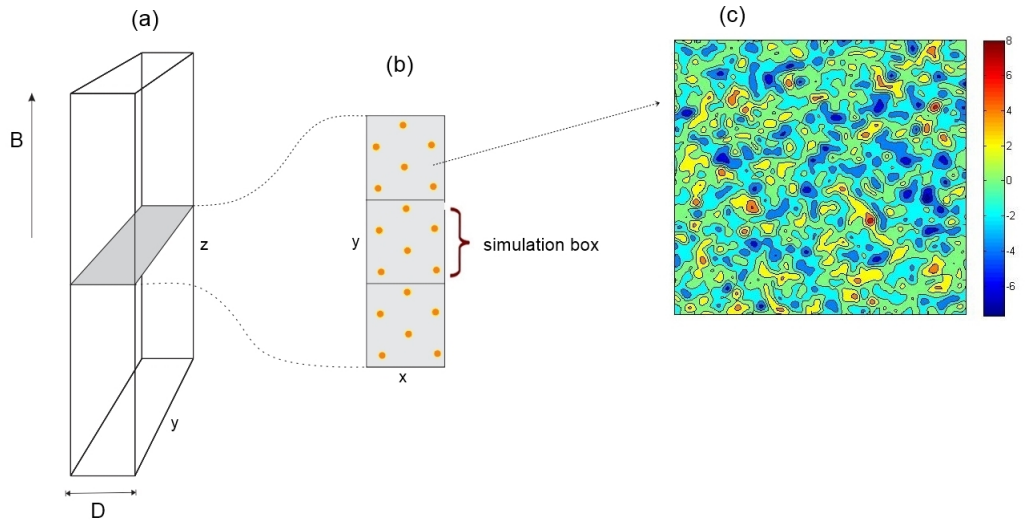

Figure 3.4: a) Infinite superconducting slab of thickness $D = 30\lambda$ under a parallel applied field. b) Simulated region. The simulation box assumes periodic boundary conditions along the y direction and is bounded by the surfaces on the x direction. c) Pinning potential representation. It was generated by a bilinear interpolation of an array of pinning with 150 points per λ. The colors bar indicates the depth of the potential wells.

The simulation box is bounded by two surfaces on the x-axis, at $x = 0$ and $x = 30\lambda$, and periodic boundary conditions along the y-axis are used in order to simulate the infinite dimension (Fig 3.4.b.). The two-dimensional dynamics is determined by the Langevin equation (Eq. 2.46), which for the i^{th} vortex can be written as

$$\eta \mathbf{v}_i = -\nabla \epsilon(\mathbf{r}_i) - \nabla U_p(\mathbf{r}_i) + \sum_j \mathbf{f}_{ij}(\mathbf{r}_{ij}) + \Gamma_i(T,t), \tag{3.8}$$

where $\epsilon(\mathbf{r}_i)$ represents the self and Meissner energies (Eq. (3.5)), and $\sum_j \mathbf{f}_{ij}(\mathbf{r}_{ij})$ is the contribution of the interaction forces between the vortices ($\mathbf{f}_{ij}$ is given by Eq. (2.37)).

To simulate the vortex-pinning interaction, we modelled a pinning potential, $U_p(x,y)$, which consists in a superposition of a large number of Gaussian potential wells, $u_p = -\epsilon_0 U_0 \exp[(x^2+y^2)/2\xi^2]$, randomly distributed throughout the sample (see e.g. [41]), where U_0 is the root-mean-square height of the pinning potential. In this way the vortices move through a resultant potential that resembles a rough surface (Fig. 3.4.c), where the value of U_0 determines if it will be strong or weak pinning.

The simulation consists in integrating de Langevin equation for each vortex inside the sample, which we are representing by a simulation box with size $L_x = D = 30\lambda$

and $L_y = 30\lambda$. In our simulation we used $\xi = 0.05\lambda$, that implies in $\kappa = 20$, which is close to some materials (e.g., Nb_3Sn, Nb_3Ge and V_3Si), and can be treated within the high kappa approximation. Starting from the Meissner state, with $H = 0$ and zero vortices, the field is increased to a chosen value greater than the entry field, but much less than H_{c2}, and then, it is decreased down to zero again in order to complete a half loop of a magnetization curve (Fig. 3.5). The penetration process is performed by the following steps: at each time step, a position (x_0, y_0) is randomly chosen, where $x_0 = \xi$ or $x_0 = D - \xi$ and $0 < y_0 < L_y$. We then calculate the resultant force that would act on the vortex if it were positioned at (x_0, y_0), i.e., the self-force plus Meissner force, which constitute the surface barrier, added to the interaction force due to all vortices inside the sample. If this force has component f_x pushing the vortex into the sample, a vortex is added at (x_0, y_0), otherwise it is rejected and the dynamics proceeds with the same number of vortices (N). If an already accepted vortex, in some step of time, assumes the position $x < \xi$ or $x > D - \xi$, it will be removed from the dynamics, which continues with $N - 1$ vortices. Since $D \gg \lambda$, for $x > \xi$, the Meissner field is given by $b_M \simeq \mu_0 H(e^{-x/\lambda} + e^{-(D-x)/\lambda})$. In the high kappa approximation (Sec. 2.4.3) the induced magnetic field of the vortex is given by $b(r) = (\phi_0/2\pi\lambda^2)K_0(\sqrt{r^2 + 2\xi^2}/\lambda)$, which also decay exponentially for $r \gg \lambda$. Thus, the forces acting on the system are all short-range, and we can assume a cutoff distance for the interactions, that we chose as $R_{cutoff} = 10\lambda$ (where it was verified that for higher values of R_{cutoff} the changes on the dynamics are negligible). Note that we are using the Clem approximation $r \longrightarrow \sqrt{r^2 + 2\xi^2}$ in order to avoid the divergence of $b(r)$ near the vortex cores. In this chapter we also assume zero temperature, $T = 0$, to avoid the flux creep effect and focus on static critical state profiles. Accordingly, the thermal shaking term of the Langevin equation can be discarded.

The integration of the Eq. (3.8) (with $T = 0$) is numerically solved by discretizing the time variable, t, in small steps of size dt (in our case $dt = 0.001\eta\lambda^2/\epsilon_0$) and evaluating the time dependent functions on the new time $t' = t + dt$. This procedure corresponds to the so-called Euler method, usually used to solve differential equations numerically. Thus, the position of the i^{th} vortex as a function of time is simply given by

$$\mathbf{r}_i(t_{n+1}) = \mathbf{r}_i(t_n) + \mathbf{v}_i(t_n)dt \tag{3.9}$$

where $n = 0, 1, 2, 3...$ represents the number of steps of time. The simulations were performed for different intensities of the pinning potential: $U_0 = 0.000$; $U_0 = 0.002$;

$U_0 = 0.004$; $U_0 = 0.008$; $U_0 = 0.016$; $U_0 = 0.032$ and $U_0 = 0.064$, covering the strong and weak pinning domains (as shown in Fig.3.5).

3.2.1 *Results and discussion*

We increased the applied field in steps of $\Delta H = H_0$, where $H_0 = \phi_0/2\pi\mu_0\lambda^2$, with a time step Δt carefully chosen such that after each Δt the configuration is stabilized. In accordance with Eq. (3.7), for $\xi = 0.05\lambda$, $H_{en} \simeq 10.4H_0$. Fig. 3.5 shows the magnetization curves obtained in the simulations for different values of U_0.

The flux density profiles, $B(x)$, obtained during the simulations for $U_0 = 0.016$ are presented in Fig. 3.6.a, where we took the average value of the flux density in the y-direction for each chosen value of x. Observe that the density of vortices has maximum values near the surfaces and decays as soon as it approaches the middle of the sample, in agreement with the classical critical state models.

Note that the critical current density is given by taking the derivative of the flux density profiles with respect to the x-coordinate. Fig. 3.6.b shows $J_c(B)$ derived from Fig. 3.6.a. Before taking the derivative, we took the average value of the flux evaluated at symmetrical positions with respect to the sample center in order to reduce noise.

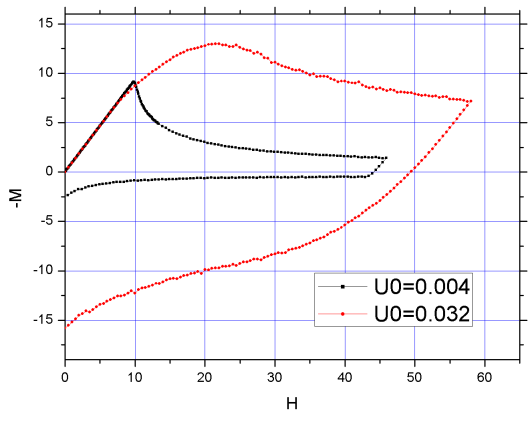

Figure 3.5: Simulation result: magnetization as a function of the applied field, H, for different values of U_0. Comparing with Fig. 2.7 we easily classify $U_0 = 0.004$ and $U_0 = 0.032$ as weak and strong pinning, respectively.

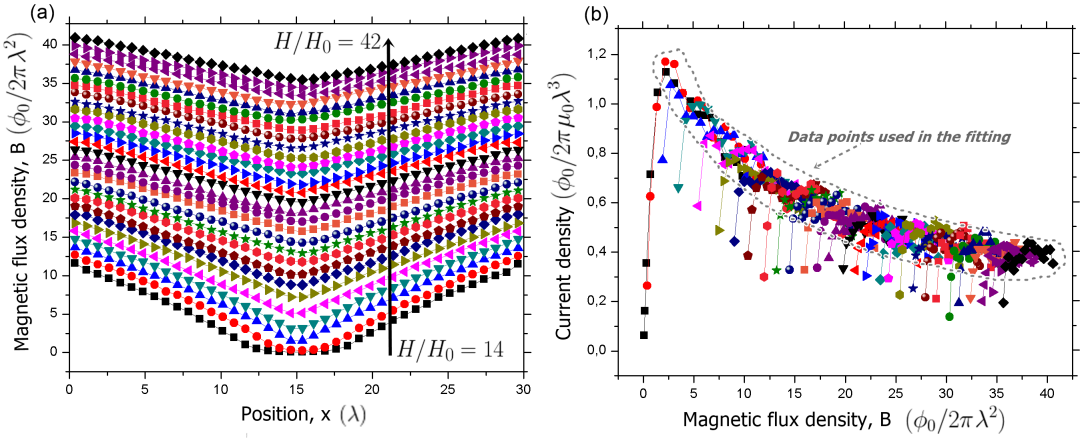

Figure 3.6: Simulation results: a) Flux density profiles for some values of H. The arrow indicates an increasing of the applied field from $H = 14H_0$ to $H = 42H_0$ in steps of $\Delta H = H_0 = \phi_0/2\pi\mu_0\lambda^2$. Note that the inclination of each flux density profile give us the local critical current density. b) Current density as a function of B . The points outside the dashed region represent the change of concavity of the flux density profiles at the center of the sample and will be disregarded from the numerical fit.

Note that the flux density profiles have greater slope in the central part of the sample, where the value of B is small, than near the surfaces where B is larger, which implies in a current density that decreases as B increases.

To check which critical state model best describes the system, we numerically fitted (for each model of table 2.1) the data points indicated in Fig. 3.6.b. The results are shown in Fig. 3.7. Observe that the Bean model is not an accurate approximation for the critical state that we obtained and, among the studied models, the model of Kim had the best fitting result. This model, proposed by Kim et al,1963 [42, 43]), was deduced empirically for high-field superconducting materials as Nb_3Sn and 3Nb-Zr. It also had satisfactory results from simulations (Richardson et al,1994 [44]) of an unidimensional vortex system, without surface effects. Our simulation describes the physical problem in a more realistic approach when compared with [44] and other numerical results known in literature, and also confirms that the Kim model presents the most satisfactory results among the studied models.

Now, let us look at what happens near the surfaces. In our simulations we observed a peculiar phenomenon: regions with no vortices nearby the surfaces appear for some pinning potentials and applied fields.

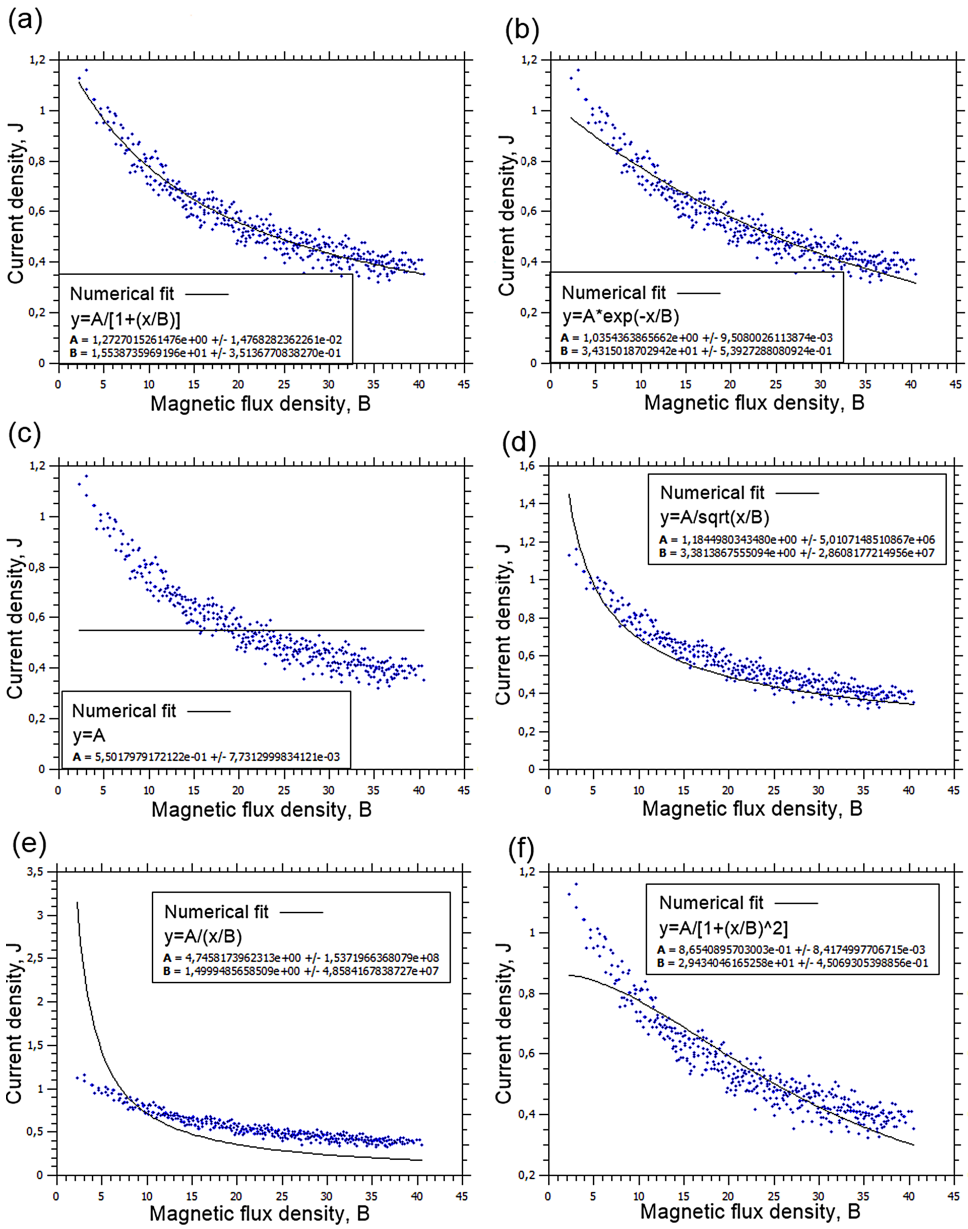

Figure 3.7: Numerical fit of the data points indicated in Fig 3.6.b for each critical state model of table 2.1. (a) Kim (b) Exponential (c) Bean (d) Square root (e) Fixed pinning (f) Quadratic. Observe that the Bean model is not an accurate approximation for our sample and, among the studied models, the model of Kim had the best fitting.

J. Clem [45] predicted these so-called *flux free regions* studying the Gibbs free energy for the Bean-Livingston surface barrier for the case of a homogeneous (pin-free) slab with a flux distribution in the sample. Using a continuum approximation, he predicted that the thickness of the flux free regions, x_{ff}, for homogeneous superconductors,

follows the expression: $x_{ff} = \lambda \cosh^{-1}(H/B)$, where B is the total magnetic field inside the sample. Our simulation results for x_{ff} are sketched in Fig 3.8. Note that the thickness of the flux free regions tends to ξ, independent of the applied field, when U_0 assumes values greater than 0.064, and the surface barrier has limited influence compared with the pinning forces. But, for weak pinning, it becomes relevant.

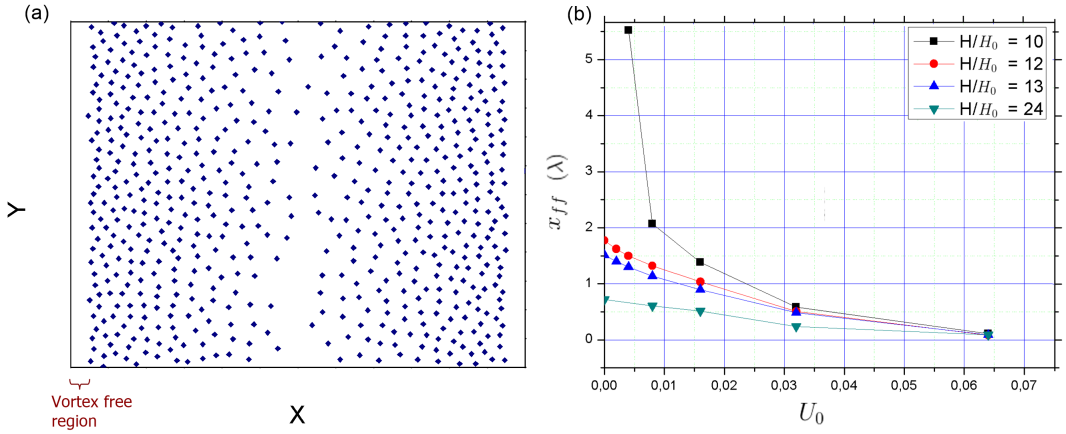

Figure 3.8: Simulation results: a) Vortices positions for $U_0 = 0.008$. The flux free regions are indicated. b) x_{ff} in function of U_0 for some different values of H. Observe that x_{ff} decays for high fields and strong pinning. Note That for $H = 10H_0$, x_{ff} diverges when $U_0 = 0$, since in that condition the entry field is greater than $10H_0$ and there is no vortex inside the sample. The values of U_0 were specified in pag. 73 .

Due to the surface interaction, the resultant force acting on the penetrating vortex, $f_x(\xi)$, is weak for H close to H_{en} (zero for $H = H_{en}$). Therefore, when the number of vortices inside the superconductor is large enough, the repulsive force from the inside vortices can be sufficient to make $f_x(\xi) < 0$ and the vortices can not penetrate anymore. The Fig. 3.9 shows the flux density profiles for $U_0 = 0.008$. Observe that in this case the flux density decays abruptly in the flux free regions before following the Kim model. In these regions it assumes only the Meissner field, since there is no vortex over there.

Our simulation results are in agreement with the Kim model for all studied values of $U_0 \neq 0$. Also our results agree with the Clem expression for x_{ff} when $U_0 = 0$, confirming the predicted flux free regions and its dependence on H proposed by Clem's microscopic model. They also showed that x_{ff} depends on the pinning level and for which values of U_0 the surface effects are relevant or not, as well as the influence of the surface effects on the critical state profiles.

Other phenomenon that can be studied here is the time evolution of the flux front and how it behaves for different values of pinning. Let us define the front position

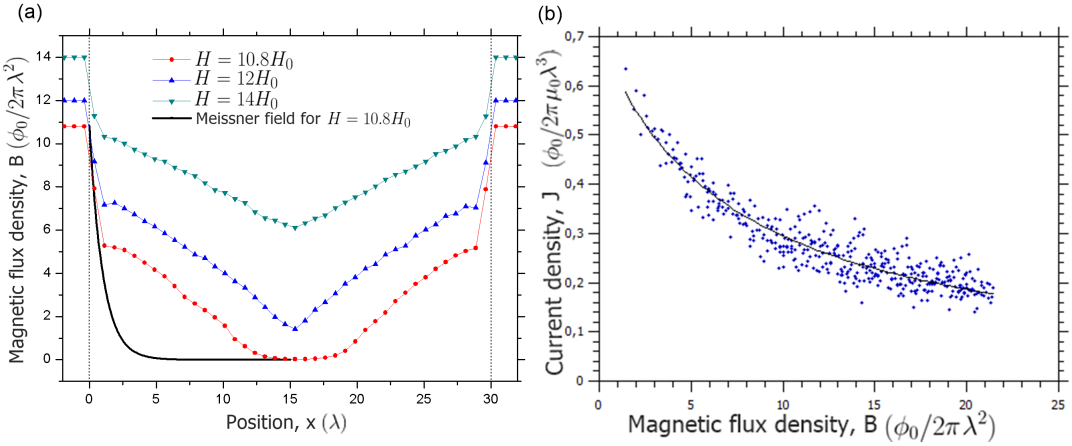

Figure 3.9: Simulation results: a) Flux density profiles for U_0 = 0.008. The surface effects induce an abruptly decay on the critical state profiles near the surface. Note that the size of the flux gap near the surface decrease for high fields, when the flux free regions are smaller. For $x > x_{ff}$ and $x < D - x_{ff}$, it follows the Kim model. b) Numerical fit confirmation of the Kim model for the U_0 = 0.008 flux density profiles.

as the x coordinate of the most advanced vortex, which we are going to call x_p. For strong pinning, it is harder for the vortex to reach the middle of the sample, since it gets stuck on the pinning sites. The flux front evolution for the different values of U_0 is shown in Fig. 3.10.a.

The flux front grows initially with time as approximately $t^{0.6}$, and eventually saturates at long times to a value x_p^* , which depends on the pinning potential. Note that the initial dependence on t does not change for any chosen value of U_0. In Fig. 3.10.b we show that this initial velocity also does not change for different values of the applied field. The temporal depence of x_p, within the used boudary conditions, was expected to be $t^{1/2}$, since in these conditions, the flux front penetration is described by the diffusion equation (see *Bryskin et al,1993* [46] *and Gilchrist et al,1994* [47]). Simulations of the flux front temporal dependence were also performed by *Moreira et al* [48]. In that case, an injection of magnetic flux was simulated by concentrating a number of flux lines (depending on the boundary conditions) at the beginning of the simulation in a small strip, parallel to the y direction. Their simulation results for the flux front propagation also fit well with the temporal dependence $x_p \propto t^{1/2}$. However, none of the cited works considered surface barriers, which are perhaps causing this difference in the initial

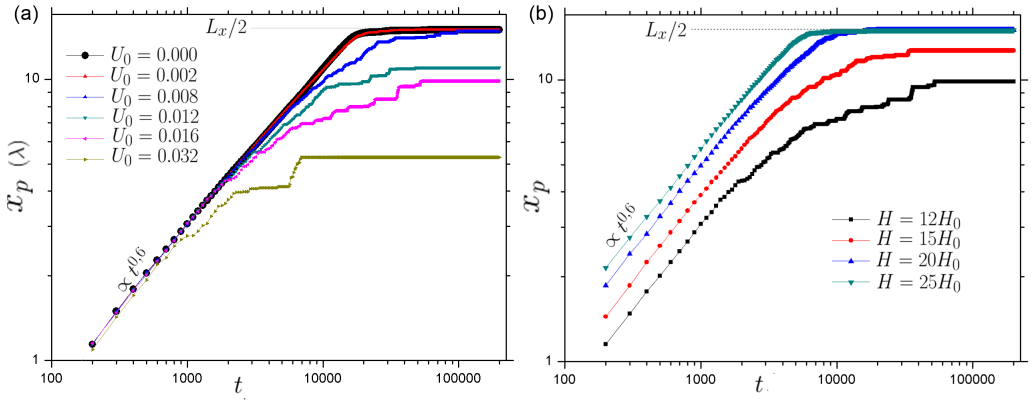

Figure 3.10: Simulation results: a) Flux front position in function of time for $H = 12H_0$ with different values of U_0. x_p grows initially with time as approximately $t^{0.6}$, and eventually saturates at a distance x_p^* from the surfaces that decreases when U_0 increases. b) Flux front position in function of time for $U_0 = 0.016$ with different values of H. Note that x_p grows initially with time as $t^{0.6}$ independently of the pinning value or applied field.

velocity of the observed flux front. However, this assumption needs a more detailed study, not performed in this work. One possible attempt consists in simply simulate the same flux penetration process with and without the surface barrier and verify if the temporal dependence of x_p changes.

4 Conformal Vortex Crystals

In this chapter we investigate the possible ordered structures that can be formed by nonuniform vortex distributions in a type-II superconductor. In situations of uniform density, the system of vortices converges to a minimum energy structure which tends to be ordered as a triangular lattice (Abrikosov lattice). However, in situations where the vortices may form nonuniform distributions, due to variations in sample thickness, interactions with material inhomogeneities, among other ways, the Abrikosov lattice does not satisfy the minimum energy condition. The question is whether the nonuniform vortex distribution assumes a structure of small domains of different densities, i.e., a nonuniform glass, or if a new ordered structure emerges. In this chapter we review the concept of conformal crystals and investigate the possibilities to observe this kind of structure in an arrangement of superconducting vortices, and whether it is an energetically favourable configuration. We perform numerical simulations and propose a simple method to calculate the external potential capable of equilibrating the conformal structures. Finally, we discuss in detail the properties of the observed configurations and suggest possible experiments to observe them.

4.1 Conformal crystals: general properties

4.1.1 The gravity rainbow experiment

In 1989, experimenting with a system of magnetized spheres, P. Pierański [49] observed a peculiar nonuniform ordered structure. This structure, whose properties will be discussed during this chapter, motivated the study of the so-called conformal crystals . The experiment was performed as follows: a few hundred steel spheres, of diameter $\delta = 1mm$, were placed within a flat, rectangular box bounded by two sheets of glass (Fig. 4.1.a). The system was subjected to a perpendicular magnetic field produced by a pair of Helmholtz coils, such that the magnetic moment induced in each sphere made

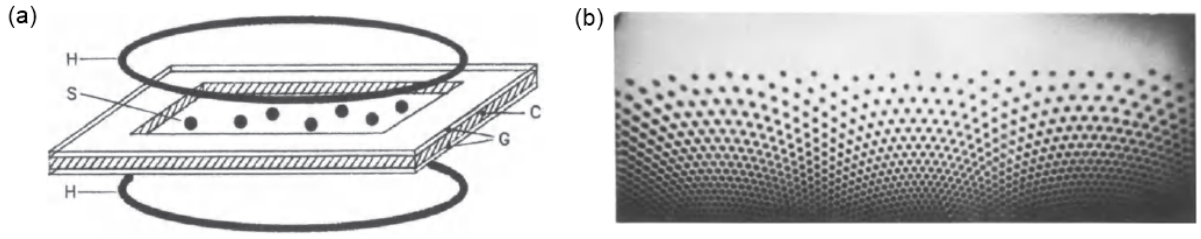

Figure 4.1: a) Experimental set-up. G- glass plates; C-cardboard spacer; S-steel spheres; H-Helmholtz coils. b) Gravity rainbow configuration. Typical final configuration of the steel spheres observed in the experiment (figures taken from [49]).

them repel each other with a repulsive potential, $V(r)$, given by the magnetic dipole interaction, $V(r) \sim 1/r^3$. When the box surface was oriented horizontally, the spheres tended to form a regular hexagonal lattice, except for some deformations due to the rectangular geometry of the box. Then, the system was slightly tilted in order to include a gravitational contribution on the spheres motion. The gravitational field pulls all spheres to one side of the box. In this situation, the hexagonal lattice is no longer the minimum of energy, and a nonuniform sphere distribution arises. Fig 4.1.b shows one of the observed structures (after a delicate shaking in order to help the system to find a minimum energy structure). This exotic/beautiful configuration was named by the author as *gravity rainbow*.

Analysing the Fig 4.1.b, one can note that the angles at which the lattice lines cross each other stay always close to $\pi/3$ (as in the hexagonal lattice). It was this angle conservation property that led the author to search for a conformal transformation which maps the gravity rainbow configuration to a uniform hexagonal lattice. As we shall see below, among the conformal transformations, the logarithm map is the only one that suits this purpose.

4.1.2 Conformal lattices

Conformal mapping is a well-studied theme in complex analysis, where it is defined as a mathematical function that transforms a number of the complex plane $z = x + iy$ to another complex number $w(z) = u(x, y) + iv(x, y)$, such that the angle between any two curves that intersect z is preserved. The first experiments on conformal crystals

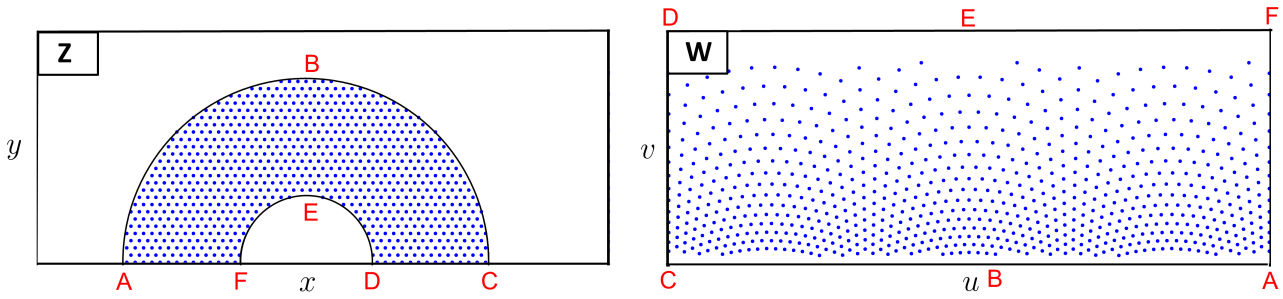

Figure 4.2: **Left:** A semiannular section of the regular hexagonal lattice on the z plane. **Right:** The conformal mapping of the left figure under the transformation $w(z) = (1/i\alpha)\ln(i\alpha z)$ with $\alpha = \pi/L$ in order to fit the semiannular geometry (the specific value of α will be discussed later in Eq. (4.48)). The letters in red are guides to identify where each region is mapped

indicated the conformal logarithm map $w(z) = (1/i\alpha)\ln(i\alpha z)$ of the regular hexagonal lattice as a possible solution to explain the gravity rainbow configuration (Fig. 4.2).

The perfect or strictly conformal crystal (Rothen *et al. 1993* [50] and *1995* [51]) has to fulfill some conditions to stay in accordance with the analyticity of the conformal mapping that defines it. In this section we review the general properties of conformal structures (where some reference works can be found in [50–54]) by reproducing the procedures used to calculate the mechanical equilibrium of conformal crystals (see [51]). This review will be useful to support the discussion on the next section.

First, consider a group of pointlike particles interacting through isotropic, power law forces and arranged in a regular hexagonal lattice. Let us analyse how the system behaves under a conformal mapping and what conditions a group of particles has to satisfy to be considered a conformal crystal.

Now, consider an arbitrary conformal transformation, given by

$$w = f(z) = u(x, y) + iv(x, y), \tag{4.1}$$

which maps a perfect hexagonal lattice from the z-plane to a conformal lattice on the w-plane. Due to the transformation, the distances between the particles will be changed according to the metric of the transformed space, given by

$$ds_w^2 = du^2 + dv^2, \tag{4.2}$$

where we can rewrite du and dv as

$$du = \frac{\partial u}{\partial x}dx + \frac{\partial u}{\partial y}dy \quad ; \quad dv = \frac{\partial v}{\partial x}dx + \frac{\partial v}{\partial y}dy. \tag{4.3}$$

$f(z)$ is said to be conformal if, and only if, f is an analytic function of z, i.e., $f(z)$ has to satisfy the Cauchy–Riemann relations [55]

$$\frac{\partial u}{\partial x} = \frac{\partial v}{\partial y} \quad , \quad \frac{\partial u}{\partial y} = -\frac{\partial v}{\partial x}. \tag{4.4}$$

In this way, substituting Eq.(4.3) into Eq.(4.2) and using the Cauchy relations, one can find that

$$ds_w^2 = \left|\frac{dw}{dz}\right|^2 ds_z^2, \tag{4.5}$$

where $ds_z^2 = dx^2 + dy^2$ is the metric of the original space. Note that Eq.(4.5) also implies in a relation between the elements of area of each space, given by $da_w = |dw/dz|^2 da_z$. Consequently, since the local density of particles is given by the number of lattice sites per unit area, the conformal lattice presents a density of particles given by

$$n_w = n_z \left|\frac{dz}{dw}\right|^2, \tag{4.6}$$

where n_z is the density of particles of the original lattice. For a hexagonal lattice $n_z = 2/\sqrt{3}b^2$, where b is the distance between the nearest neighbours (the edge of the hexagons).

Note that the derivative of w with respect to z, that we are going to define as $\zeta(w) \equiv dw/dz$, contains all information about the geometry of the conformal lattice around w. Rothen *et al.* [51] refer to $\zeta(w)$ as the *complex distortion*, which can be rewritten as

$$\zeta(w) = |\zeta| e^{i\varphi}, \tag{4.7}$$

where φ is a complex phase. Now, let Δz be a vector on the z plane connecting two neighboring points, and Δw the same vector through the transformation $w = f(z)$,

$$\begin{aligned} \Delta z &= |\Delta z| e^{i\varphi_z}, \\ \Delta w &= |\Delta w| e^{i\varphi_w}. \end{aligned} \tag{4.8}$$

Expanding Δw with respect to Δz we obtain

$$|\Delta w|e^{i\varphi_w} = \Delta w = \frac{dw}{dz}\Delta z + O(\Delta z^2). \tag{4.9}$$

Remember that $dw/dz = \zeta(w)$. Considering Δz much smaller than the characteristic length in which the function $w(z)$ changes appreciably and using Eqs.(4.7) and (4.8), Eq.(4.9) becomes

$$|\Delta w|e^{i\varphi_w} \approx |\zeta||\Delta z|e^{i(\varphi_z+\varphi)} \tag{4.10}$$

Therefore, φ is directly related to the angle at which the hexagon of the conformal lattice has been turned with respect to the corresponding hexagon of the original lattice, and $|\zeta|$ indicates the dilatation of the distances between the particles in the neighborhood of w.

4.1.3 *Strictly conformal crystals*

A group of particles is said to form a strictly conformal crystal (SCC) if each particle is positioned exactly on the conformal lattice sites. Consider a pair of particles, that we are going to call i and j, belonging to a SCC and interacting through an isotropic, power law force, F_{ij}, given by

$$F_{ij} = A\frac{w_j - w_i}{|w_j - w_i|^{k+2}}, \tag{4.11}$$

where k is a fixed exponent and A is a positive constant. Let us calculate the total force that the particles positioned at the vertices of a conformally transformed hexagon $\{w_l\}$, $l = 1, 2, ..., 6$ exert in a particle positioned at the center of the same hexagon (Fig. 4.3(right)).

The original hexagon, on the z plane, is illustrated in Fig. 4.3(left), where we denote z_l as the vertices positions and z as the central position. Note that we can rewrite z_l as

$$z_l = z + be^{i\alpha_l}, \tag{4.12}$$

where b is the distance between the center and the vertices of the hexagon and $\alpha_l = l\pi/3$, $l = 1, 2, ..., 6$. In other words, $\Delta z = z_l - z = be^{i\alpha_l}$. In what follows we assume b much smaller than the characteristic length, r, in which the function $w(z)$ changes appreciably, i.e.,

$$\frac{1}{|w|}\left|\frac{dw}{dz}\right| \approx \frac{1}{r} \quad \text{and} \quad \frac{b}{r} \ll 1. \tag{4.13}$$

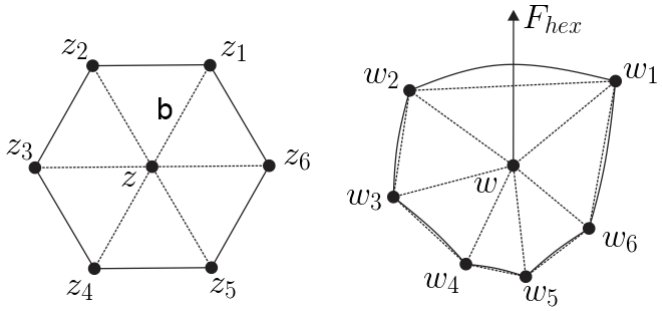

Figure 4.3: Left: Original hexagon on the z plane. Right: example of a conformally transformed hexagon on the w plane .

Similar to Eq. (4.9), we can expand Δw as

$$w_l - w = \Delta w = \frac{dw}{dz}\Delta z + \frac{1}{2}\frac{d^2w}{dz^2}(\Delta z)^2 + \ldots \tag{4.14}$$

Defining $\eta(w) \equiv d^2w/dz^2 = |\eta|e^{i\psi}$ and using Eq. (4.12), Eq.(4.14) can be rewritten as

$$w_l - w = |\zeta|be^{i(\alpha_l+\varphi)} + \frac{1}{2}|\eta|b^2e^{i(2\alpha_l+\psi)} + \ldots \tag{4.15}$$

and,

$$\frac{1}{|w_l - w|^{k+2}} = \left[\frac{1}{b|\zeta|}\right]^{k+2}\left[1 - \frac{k+2}{2}b\left|\frac{\eta}{\zeta}\right|\cos(\alpha_l + \psi - \varphi)\right] + \ldots, \tag{4.16}$$

where we used the binomial expansion. The force acting on the central particle due to the particle positioned in w_l can be written as

$$F_l = A\frac{w - w_l}{|w - w_l|^{k+2}} = F_l^u + iF_l^v. \tag{4.17}$$

Therefore, the total force due to all particles located on the hexagon $(w_1, w_2, \ldots, w_6)$ is given by $F_{hex} = \sum_{l=1}^{6} F_l$. Using Eqs. (4.15), (4.16) and (4.17), we easily obtain

$$F_{hex} = \sum_{l=1}^{6} F_l = -A\sum_{l=1}^{6}\left[\frac{1}{b|\zeta|}\right]^{k+1}\left[e^{i(\alpha_l+\varphi)} + \frac{b|\eta|}{2|\zeta|}e^{i(2\alpha_l+\psi)}\right]\left[1 - \frac{k+2}{2}b\left|\frac{\eta}{\zeta}\right|\cos(\alpha_l + \psi - \varphi)\right] + \ldots \tag{4.18}$$

Since $\sum_{l=1}^{6} e^{i\alpha_l} = \sum_{l=1}^{6} e^{i2\alpha_l} = 0$, the leading nonvanishing term of Eq. (4.18) corresponds to the product $e^{i(\alpha_l+\varphi)}\cos(\alpha_l + \psi - \varphi)$, i.e.,

$$F_{hex} = A\frac{k+2}{2}\frac{|\eta|}{b^k|\zeta|^{k+2}}\sum_{l=1}^{6}\cos(\alpha_l + \psi - \varphi)e^{i(\alpha_l+\varphi)} + O(b/r) \tag{4.19}$$

Rewriting the cosine in the form $\cos(\theta) = (e^{i\theta} + e^{-i\theta})/2$ and calculating the summation, Eq. (4.19) results in

$$F_{hex} = A\frac{k+2}{2}\frac{|\eta|}{b^k|\zeta|^{k+2}}3e^{i(2\varphi-\psi)} + O(b/r) = F^u_{hex} + iF^v_{hex}. \tag{4.20}$$

Looking at Eq.(4.20), we can note that F_{hex} depends explicitly on the specific hexagon orientation, φ. However, such explicit dependence can be avoided if we rewrite F_{hex} in terms of the density of particles. For this, let us try to write down the density gradient of the SCC, ∇n_w. Defining the gradient operator on the complex w-plane as $\nabla = \partial/\partial u + i\partial/\partial v$ and using Eq (4.6), we have

$$\nabla n_w = n_z\frac{\partial}{\partial u}\left|\frac{dz}{dw}\right|^2 + in_z\frac{\partial}{\partial v}\left|\frac{dz}{dw}\right|^2, \tag{4.21}$$

where,

$$\frac{\partial}{\partial u}\left|\frac{dz}{dw}\right|^2 = \frac{\partial}{\partial u}\left[\frac{dz}{dw}\left(\frac{dz}{dw}\right)^*\right] = \frac{\partial w}{\partial u}\frac{d^2z}{dw^2}\left(\frac{dz}{dw}\right)^* + c.c. \tag{4.22}$$

Here, a^* is the complex conjugate of a. Using that $\partial w/\partial u = 1$, we obtain

$$\frac{\partial}{\partial u}\left|\frac{dz}{dw}\right|^2 = \frac{d^2z}{dw^2}\left(\frac{dz}{dw}\right)^* + \left[\frac{d^2z}{dw^2}\left(\frac{dz}{dw}\right)^*\right]^*. \tag{4.23}$$

In the same way,

$$\frac{\partial}{\partial v}\left|\frac{dz}{dw}\right|^2 = i\frac{d^2z}{dw^2}\left(\frac{dz}{dw}\right)^* - i\left[\frac{d^2z}{dw^2}\left(\frac{dz}{dw}\right)^*\right]^*. \tag{4.24}$$

Therefore, using Eqs. (4.21), (4.23), (4.24) and $n_z = 2/\sqrt{3}b^2$ for a hexagonal lattice, we obtain

$$\nabla n_w = \frac{4}{\sqrt{3}b^2}\left[\frac{d^2z}{dw^2}\left(\frac{dz}{dw}\right)^*\right]^*, \tag{4.25}$$

where,

$$\frac{d^2z}{dw^2} = \frac{d}{dw}\left(\frac{dz}{dw}\right) = \frac{dz}{dw}\left[\frac{d}{dz}\left(\frac{dz}{dw}\right)\right] = -\frac{d^2w}{dz^2}\left(\frac{dw}{dz}\right)^{-3}. \tag{4.26}$$

Finally, using that $d^2w/dz^2 = |\eta|e^{i\psi}$ and $dw/dz = |\zeta|e^{i\varphi}$, the density gradient of the SCC can be written as

$$\nabla n_w = -\frac{4}{\sqrt{3}b^2}\frac{|\eta|}{|\zeta|^4}e^{i(2\varphi-\psi)}. \tag{4.27}$$

In the same way we can obtain the expression for $\nabla(n_w^{k/2}) = (k/2)n_w^{(k/2)-1}\nabla n_w$. Comparing with Eq. 4.20, after a simple calculation, we obtain

$$\vec{F}_{hex} = -A\frac{(k+2)}{k}\frac{3^{(k+4)/4}}{2^{(k+2)/2}}\vec{\nabla}(n_w^{k/2}), \tag{4.28}$$

where now we are going to consider the complex plane as the physical xy-plane, i.e., $\vec{a} = (a^u, a^v)$ represents a vector in Cartesian coordinates. Observe that now F_{hex} depends only on the kind of interaction force (given by A and k) and the density gradient of the SCC.

Now, let us recap what we have done so far. Eq. (4.28) represents the force acting on a particle of the SCC due to its six nearest neighbors. To compute the contribution of the remaining particles we can decompose the lattice in concentric hexagons of different sizes and orientations, as illustrated in Fig. 4.4. Thus, the contribution of each hexagon will be given by Eq. (4.28) rescaled for the correspondent sizes. A hexagon in which the distance, d, from the center differs from b by a multiplicative factor, α, i.e., $d = \alpha b$, has contribution $(1/\alpha^k)F_{hex}$ (see Eq. (4.20)). For example, defining the families of hexagons $H_1, H_2...$ as illustrated in Fig 4.4, the first family, H_1, has only one hexagon which exerts a force F_{hex} on the central particle; the second one, H_2, contribute with two hexagons, one with side $d = 2b$ and the other with $d = \sqrt{3}b$, so that the contribution of H_2 to the total force, F_{int}, is given by $(1/2^k)F_{hex} + (1/3^{k/2})F_{hex}$. In the same reasoning, the family H_n has n hexagons with sizes between $d = (\sqrt{3}/2)nb$ and $d = nb$, such that, the contribution of the family H_n, for $n > 2$, to the total force is not larger than $n[1/(n\sqrt{3}/2)^k]F_{hex}$. In this way , the total force acting on the central particle can be expressed as

$$\vec{F}_{int} = f(k)\vec{F}_{hex}, \tag{4.29}$$

where,

$$1 < f(k) < 1 + \frac{1}{2^k} + \frac{1}{3^{k/2}} + \sum_{n=3}^{\infty} n\left(\frac{2}{n\sqrt{3}}\right)^k \equiv g(k). \tag{4.30}$$

Note that $g(k)$ converges only for $k > 2$. Looking at Eq. (4.28), we can rewrite the total force as

$$\vec{F}_{int} = -AJ(k)\vec{\nabla}(n_w^{k/2}) \quad , \quad k > 2, \tag{4.31}$$

where,

$$J(k) \cong \frac{(k+2)}{k}\frac{3^{(k+4)/4}}{2^{(k+2)/2}}g(k) \quad , \quad k > 2. \tag{4.32}$$

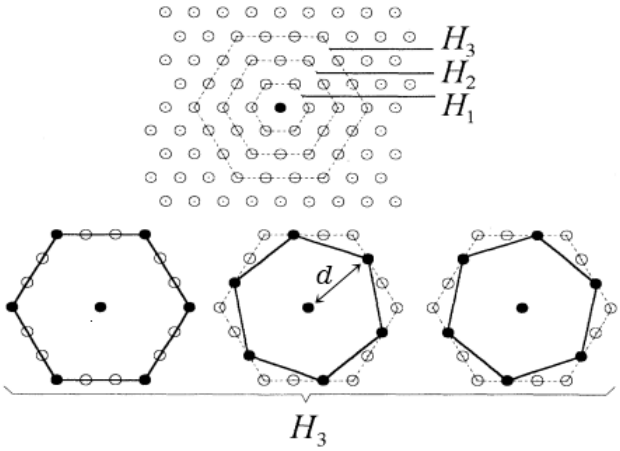

Figure 4.4: Schematic representation of the families of hexagons that are centred at the position z. Note that H_n contains n hexagons with sizes between $d = (\sqrt{3}/2)nb$ and $d = nb$. The three possibilities of H_3 are shown (figure taken from Rothen *et al* [51]).

Observe that Eq. (4.31) is a reasonable approximation for particles interacting through a short-range potential ($k > 2$), when the influence of the nearest neighbors is much larger than the influence of the further particles, and the hexagons with d/r not much smaller than 1 (condition assumed in Eq. (4.13)) have negligible influence. For example, in the gravity rainbow experiment, the magnetized spheres interact through a potential $V \sim 1/r^3$, which implies in $k = 3$. Also note that, for a finite number of particles, the summation in $g(k)$, Eq. (4.30), should also be finite.

Eq. (4.31) was calculated considering $w(z)$, and dw/dz, analytic functions of z. In this way, there must be $\varphi(w)$ such that $\zeta(w) = |\zeta|e^{i\varphi}$ is an analytic function of w. Therefore, we can write the Cauchy-Riemann relations (Eq (4.4)) as

$$\begin{aligned} \frac{\partial|\zeta|}{\partial u} &= |\zeta|\frac{\partial\varphi}{\partial v}; \\ \frac{\partial|\zeta|}{\partial v} &= -|\zeta|\frac{\partial\varphi}{\partial u}. \end{aligned} \tag{4.33}$$

From the Cauchy-Riemann relations we obtain that

$$\nabla^2 \ln|\zeta| \equiv \frac{\partial^2}{\partial u^2}\ln|\zeta| + \frac{\partial^2}{\partial v^2}\ln|\zeta| = 0. \tag{4.34}$$

Using that, apart from a constant factor $n_w = |\zeta|^{-2}$ (see Eq (4.6)), Eq. (4.34) results in

$$\nabla^2 \ln(n_w) = 0. \tag{4.35}$$

Comparing the above equation with Eq. (4.31), we also obtain

$$\nabla \cdot \left(\frac{\vec{F}_{int}}{A n_w^{k/2}} \right) = 0. \tag{4.36}$$

Eqs. (4.35) and (4.36) represent the conditions in which the internal forces and density of particles have to satisfy to stay in accordance with the analyticity of the conformal map. The external force field needed to stabilize the SCC is then determined by $\vec{F}_{int} + \vec{F}_{ext} = 0$. From Eqs. (4.31) and (4.36), we have

$$\vec{F}_{ext} = AJ(k)\vec{\nabla}(n_w^{k/2}), \tag{4.37}$$

$$\nabla \cdot \left(\frac{\vec{F}_{ext}}{A n_w^{k/2}} \right) = 0. \tag{4.38}$$

These two equations define the external force field needed to stabilize the SCC. Rothen et al [51] showed, by using numerical simulations, that Eqs (4.37) and (4.38) successfully describe the equilibrium forces on a SCC in different symmetries (planar and radial) for $V(r) \sim 1/r^3$.

Now, let us recap the results presented in this literature review: Eq.(4.35) gives us the particle density distribution of a SCC for any conformal mapping, while Eq.(4.37) gives us the external force field required to equilibrate it. However, the expression obtained for the force field (Eq.(4.37)) is quite limited, being valid only in the limit of small distances between the particles (see Eq.(4.13)) and for power law interaction forces with $k > 2$ (see Eq.(4.11)). Thus, it does not cover some important interaction laws, such as Coulomb interaction and logarithmic interaction, let alone interactions between vortices, either in bulk materials or in thin films. Therefore, a more comprehensive theory becomes necessary.

4.1.4 Strictly conformal crystals - planar symmetry

In the previous section we obtained some properties of a strictly conformal crystal for any conformal map. Now, let us consider the case in which the SCC can be stabilized by an unidirectional force field $\vec{F}_{ext} = (0, -F_v)$ compressing the particles in a hard wall located at $v = 0$ (Fig. 4.5) (the same symmetry of the gravity rainbow, produced by the

gravitational field). In this case the density of particles changes only on the v direction, and due to Eqs. (4.35) and (4.37), we obtain

$$\frac{\partial^2}{\partial v^2}\ln(n_w) = 0, \tag{4.39}$$

$$F_v = -AJ(k)\frac{\partial}{\partial v}(n_w^{k/2}), \tag{4.40}$$

Eq. (4.39) results in

$$n_w(v) = n_w(0)e^{-\beta v}, \tag{4.41}$$

where β is a positive constant. Consequently,

$$F_v = AJ(k)[n_w(0)]^{k/2}\frac{\beta k}{2}e^{-(\beta k/2)v}, \quad k > 2. \tag{4.42}$$

Therefore, to stabilize a SCC of planar symmetry, the external force field must decay exponentially. Observe that this is not the case of the gravity rainbow experiment, in which the gravitational field is constant, thus forming a non-strictly, but approximated, conformal crystal structure.

Now, let us analyse a confined and finite SCC. Consider a finite number of particles, N, forming a SCC confined in a two dimensional box of size L_uxL_v. The finite system defines the parameters of Eqs. (4.41) and (4.42). For example, $n_w(0)$ is given by the condition

$$n_w(0) = \frac{N}{\int\limits_{box} e^{-\beta v}du\,dv} = \frac{N\beta}{L_u(1-e^{-\beta L_v})}, \tag{4.43}$$

where we used Eq. (4.41) integrated on the area of the box. To fit the box boundary conditions in u direction (where could be hard walls or periodic boundary conditions), the difference on the orientation, $\Delta\varphi$, of those hexagons located at $u = L_u$ and $u = 0$ has to assume a value equal to some multiple of $\pi/3$. From Eq. (4.33) we can write

$$\frac{\partial\varphi}{\partial u} = -\frac{\partial}{\partial v}\ln|\zeta| = -\frac{\partial}{\partial v}\ln(n_w^{-1/2}) = -\frac{\beta}{2}, \tag{4.44}$$

where we used Eq. (4.41). Thus, integrating from $u = 0$ to $u = L_u$, we obtain

$$\varphi(L_u) - \varphi(0) = -\frac{\beta L_u}{2} \equiv -\frac{\pi}{3}l, \tag{4.45}$$

with $l = 1, 2, 3\ldots$. Consequently, the parameter β is also determined and the density of particles finally becomes

$$n_w(v) = n_w(0)e^{-(2\pi l/3L_u)v}. \tag{4.46}$$

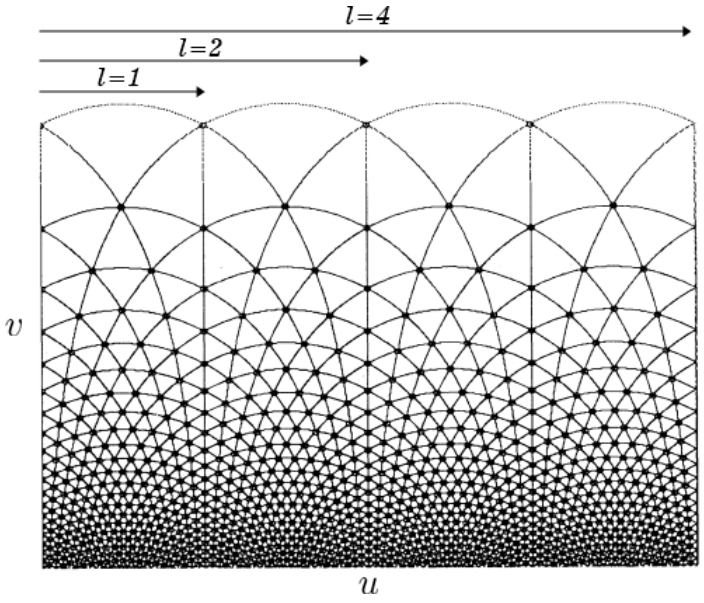

Figure 4.5: Structure of a SCC stabilized by an unidirectional force field $\vec{F}_{ext} = (0, -F_v)$. This structure can be mapped from a hexagonal lattice by the conformal map obtained in Eq. 4.48. Note that the factor l defines the number of arcs that fits into the box boundaries (figure edited from Rothen *et al* [51]).

From Eqs. (4.6) and (4.46), the conformal map has to satisfy

$$\frac{dw}{dz} = e^{-(i\pi l/3L_u)w}, \tag{4.47}$$

and then

$$w(z) = \frac{1}{i\alpha}\ln(i\alpha z), \quad \alpha = \frac{\pi l}{3L_u}. \tag{4.48}$$

Fig. 4.2 shows the conformal mapping of a semiannular section of the regular hexagonal lattice through Eq. (4.48). Note that $\alpha = \pi/L_u$ fits exactly in a semiannular section of the z plane specified by $Im(z) \geq 0$ and $r_{in} \leq |z| \leq r_{out}$. In general, the factor α gives us the size of the angular section in the z plane (Fig. 4.2) and the number of arcs in the w plane (Fig. 4.5).

4.2 Conformal vortex crystals

When scientists working on vortex physics hear about nonuniform vortex distributions one of the first things that comes to mind is the *critical state*, where, as we studied before in chapter 3, the flux penetration in an inhomogeneous superconductor results

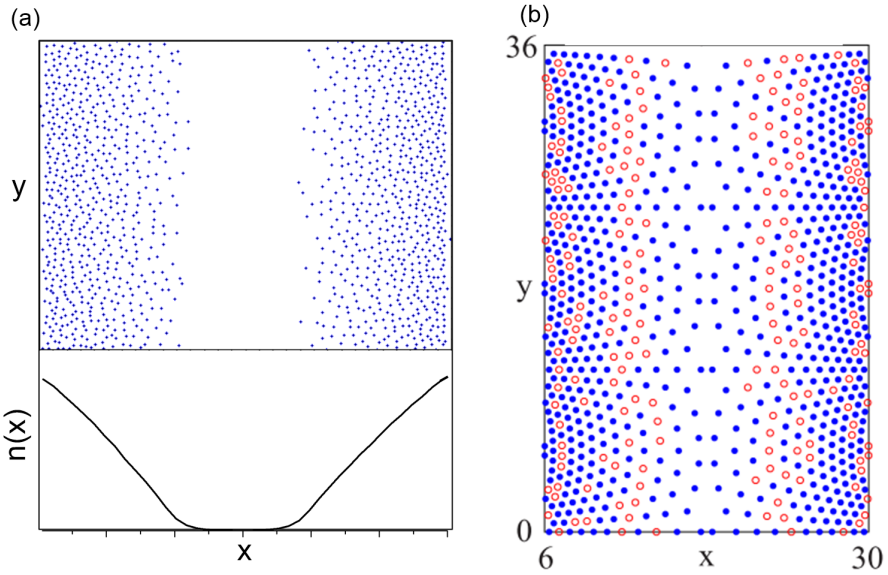

Figure 4.6: a) Simulation results for the vortex penetration in an inhomogeneous superconductor. Top: vortex positions. Bottom: Density of vortices in function of the x position. $n(x)$ is described by the model of kim. b) Conformal pinning array, figure taken from D.Ray *et al, 2014* [56]. The blue and red circles indicate the occupied (contains a vortex) and unoccupied pinning sites, respectively, for a chose applied field. Note that to form a SCC the system should have the same number of vortex as pinning sites, which must be completely filled.

in a nonuniform vortex distribution. Some authors, however, have studied conformal pinning configurations in the critical state problem. For instance, in a recent work by D.Ray et al 2014 [56], the authors used a conformal pinning array, where pinning centers were positioned at the conformal lattice positions, to analyse critical current and magnetization properties compared with other nonconformal pinning configurations. However, even in this situation the conformal vortex crystal does not appear in the critical state problem (Fig. 4.6.b). Fig. 4.6.a shows a generic result of our critical state simulations in chapter 3, where we showed that the density of magnetic flux (consequently the density of vortices) follows the model of Kim (Pag. 53) in a random pinning distribution. Note that, the exponential distribution of Eq. (4.46), which is a necessary condition to observe the SCC, does not satisfy the model of kim, since it requires a different concavity. In this way, we need a different process to find the conformal vortex crystal.

In this section we investigate the possibilities to observe conformal crystals in an arrangement of superconducting vortices. The main questions here are "Can we perform an nonuniform vortex distribution able to organize in a conformal crystal ?" and "Is the

conformal structure a minimum energy state of the vortex lattice?" Up to this point, only the Abrikosov configuration (or in specific situations the square lattice) has been considered an ordered fundamental state of the vortex lattice. In the following we used numerical simulations to try to answer these questions and to study some properties of this peculiar structure. At first, let us try to reproduce the gravity rainbow configuration with vortices.

4.2.1 *Reproducing the "gravity rainbow" with vortices*

In order to reproduce the same situation of the gravity rainbow (GR) experiment, but with superconducting vortices instead of steel balls, we performed numerical simulations, using the same dynamics discussed in the chapter 3. We consider $N = 3000$ vortices interacting with each other in a two dimensional box with periodic boundary conditions in both directions and size $L_x = 60\lambda$, $L_y = 120\lambda$, such that in the absence of external forces the system would form a triangular lattice (Abrikosov lattice). The

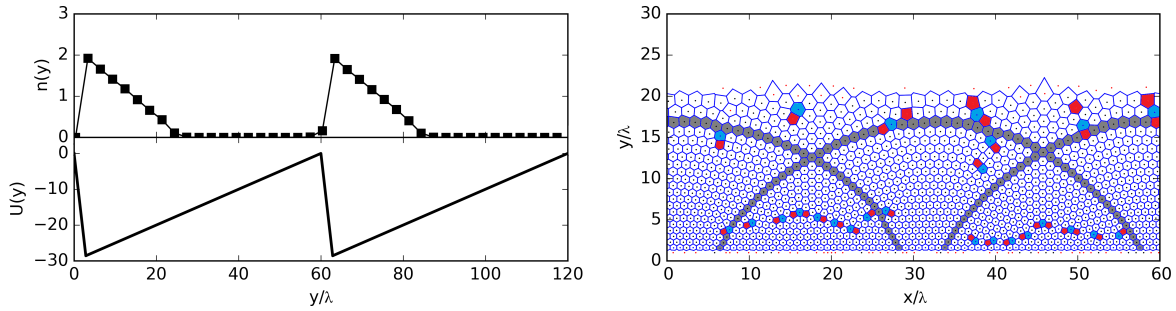

Figure 4.7: a) Top: Vortex density profile, $n(y)$, obtained in the simulations. Bottom: Potential energy used in the simulations. It was chose in order to simulate the GR problem, the soft and hard inclination regions assume the form $U(y) = a + by$ with $b = 0.5\epsilon_0/\lambda$ and $b = -10\epsilon_0/\lambda$, respectively. The value of b was chosen in such a way that the maximum force exerted by the external potential is not enough to break the cooper pairs, otherwise it could not be applied to vortices. b) Voronoy diagram of the typical minimum energy configuration observed in the simulations. The red and blue shaded polygons represent, respectively, 5-fold and 7- fold coordinated vortices (topological defects) and the gray shaded polygons are guides to the eye for better identification of the arch-like structure. The vortices are represented by the dots.

GR experiment can be characterized by three main ingredients: the particles interact repulsively; the particles are compressed against a kind of wall; and the force field is constant. The first condition is immediately guaranteed by the vortex-vortex interaction

(Eq (2.37)), and, to simulate the other two conditions, in a purely mathematical situation, we assumed a periodic sawtooth potential energy as sketched in Fig. 4.7.a.

The simulation consisted in a thermal annealing, where the system of vortices (randomly distributed) started with a temperature, T, greater than the melting temperature, T_f, of the vortex lattice (subsection 2.6.1), and was gently cooled to its lowest energy state at $T = 0$. In this situation, the integrated Langevin equation becomes (see Eq. (2.46) and Eq. (3.9))

$$\mathbf{r}_i(t_{n+1}) = \mathbf{r}_i(t_n) + \mathbf{v}_i(t_n)dt + u(t_n)\sqrt{Ddt} \tag{4.49}$$

where the last term of the right side of the Eq. (4.49) refers to the integration of the stochastic Langevin force, $\Gamma(T, t)$, which represents the thermal shaking,

$$\int_{t_n}^{t_{n+1}} dt\, \Gamma(T, t) = \eta u(t_n)\sqrt{Ddt} \tag{4.50}$$

where $u(t_n)$ is a zero-mean, unit-variance Gaussian variable and $D = 2k_BT/\eta$. The values of dt, η and other parameters are the same used in chapter 3. A detailed discussion of Eq. (4.50) can be found in [57]. The temperature steps were performed as $T = 2T_f/m$, where $m = 1, 2, 3, \ldots$ indicates the number of steps of time, $\tau = 100.000dt$, that have passed during the simulation. When $T < T_f/100$, i.e., $m > 200$, the temperature was abruptly dropped to $T = 0$ and the simulation ended. The same process was repeated several times (50 times at least). Fig. 4.7.b shows the Voronoy diagram of the typical minimum energy configuration observed in the simulations, where the gray shaded polygons are guides to the eye for better identification of the arch-like structure.

Looking back at Fig. 4.1, one can easily note that the simulation results showed in Fig. 4.7 present the same characteristics of the original GR structure. However, when we tried to reproduce the same process for vortices in thin films, where the vortex-vortex interaction potential (logarithmic interaction) is long-range (subsection 2.4.5), the vortex lattice did not form the nonuniform distribution required to observe the conformal structure (Fig. 4.8). Note that in this case the relevant length is given by the effective penetration depth $\lambda_{eff} = \lambda^2/d$, where d is the film thickness. Remember that Eq. (4.42) (force condition), obtained in the previous section, is an approximation for short-range potentials, while the Eq. (4.41)(density condition) is valid for any interaction force. In this way, how can we obtain the conformal density profile from Eq. (4.41) for any kind of interacting particles? As we shall see in the next subsection, this problem can be solved by a simple construction.

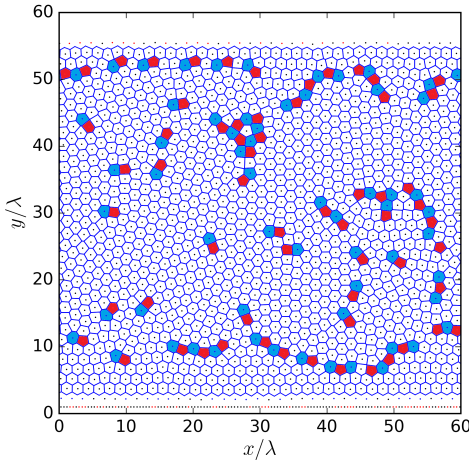

Figure 4.8: Voronoy diagram of the typical minimum energy configuration observed in the thin film simulations under the same sawtooth potential energy of the Fig. 4.7. Note that, in this case, the vortex lattice does not present the nonuniform distribution required to observe the conformal structure. The red and blue shaded polygons represent, respectively, 5-fold and 7- fold coordinated vortices (topological defects). The vortices are represented by the dots.

Now, let us pay attention to some differences in the thin film simulations compared with the bulk geometry simulated in chapter 3. At first, we can not assume a cutoff on the interaction forces since the influence of distant particles is no longer negligible. In this way, to simulate the periodic boundary condition we need to sum infinite periodic images of each vortex inside the simulation box, as illustrated in Fig. 4.9. Niels Gronbech-Jensen, 1996 [58] calculated this summation for particles interacting via a potential energy $V(r) = -\ln(r)$, where he found that the force acting on the particle 1 (see Fig. 4.9) due to the infinite images of the particle 2 is given by

$$F_{12}^{(x)} = \frac{\pi}{L_x} \sum_{n=-\infty}^{\infty} \frac{\sin(2\pi\frac{\Delta x}{L_x})}{\cosh\left(2\pi\frac{L_y}{L_x}\left(\frac{\Delta y}{L_y}+n\right)\right) - \cos(2\pi\frac{\Delta x}{L_x})}, \tag{4.51}$$

$$F_{12}^{(y)} = \frac{\pi}{L_x} \sum_{n=-\infty}^{\infty} \frac{\sinh\left(2\pi\frac{L_y}{L_x}\left(\frac{\Delta y}{L_y}+n\right)\right)}{\cosh\left(2\pi\frac{L_y}{L_x}\left(\frac{\Delta y}{L_y}+n\right)\right) - \cos(2\pi\frac{\Delta x}{L_x})} - \frac{2\pi}{L_x}\frac{\Delta y}{L_y}, \tag{4.52}$$

where Δx and Δy represent the distance between the particles. Thus, the vortex-vortex interaction can be simulated using Eqs. (4.51), (4.52).

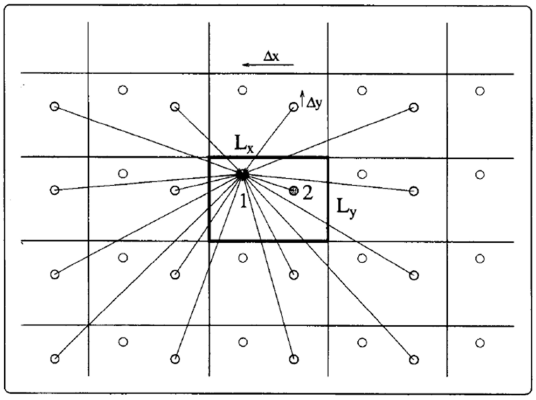

Figure 4.9: Schematic representation of two particles interacting in the simulation box (thick rectangle) with periodic boundary conditions and size $L_x x L_y$. The particle 1 interact with the infinite images of the particle 2.

4.2.2 *Strictly conformal density profile*

Consider a system of N particles interacting via a pair potential $V_{int}(\mathbf{r}, \mathbf{r}')$ and subjected to an external potential $U(r)$. The free energy of the system, $\mathcal{F}$, within the continuum approximation, can be expressed as [59]

$$\mathcal{F} = \int d\mathbf{r}\, n(\mathbf{r})\, U(\mathbf{r}) + \frac{1}{2} \int d\mathbf{r}\, d\mathbf{r}'\, n_2(\mathbf{r}, \mathbf{r}')\, V_{int}(\mathbf{r}, \mathbf{r}'), \tag{4.53}$$

where the first integral represents the self energy of each particle under the external potential $U(r)$ and the second one refers to the interaction energy between the particles. $n_2(\mathbf{r}, \mathbf{r}')$ is the two-particle distribution function. Considering that the inter-particle spacings are smaller than any other relevant length scale, n_2 can be approximated as $n_2(\mathbf{r}, \mathbf{r}') = n(\mathbf{r})n(\mathbf{r}')$. Note that, for a given $n(\mathbf{r})$, we can find the external potential that minimizes the energy by minimizing the functional $\mathcal{F}$ with respect to $n(\mathbf{r})$. This minimization results in the following condition

$$U(\mathbf{r}) = -\int d\mathbf{r}' n(\mathbf{r}') V_{int}(\mathbf{r}, \mathbf{r}') + C, \tag{4.54}$$

where C is a constant to be determined by the condition $\int d\mathbf{r} n(\mathbf{r}) = N$. Thus, from Eq. (4.54), we can calculate the external potential able to accommodate the particles, in general, or vortices, in particular, in a strictly conformal density profile just by choosing $n(\mathbf{r})$ as in Eq. (4.46).

In particular, for the cases where $n(\mathbf{r})$ changes on a scale much larger than the characteristic length of the interaction potential, Eq. (4.54) can be approximated by

$$U(\mathbf{r}) = -g(\mathbf{r})n(\mathbf{r}) \quad \text{with} \quad g(\mathbf{r}) = \int d\mathbf{r}' V_{int}(\mathbf{r}, \mathbf{r}'). \tag{4.55}$$

In bulk type-II superconductors, the vortex-vortex interaction is given by $V_{int}(\mathbf{r}, \mathbf{r}') = 2\epsilon_0 K_0(|\mathbf{r} - \mathbf{r}'|/\lambda)$ (see Eq. (2.38)). Assuming the local approximation, i.e., $n(\mathbf{r})$ changes on a scale much larger than λ, Eq. (4.55) can be used and $g(\mathbf{r})$ becomes

$$g(\mathbf{r}) = 2\epsilon_0 \int r' dr' d\theta' K_0 \left(\frac{|\mathbf{r} - \mathbf{r}'|}{\lambda} \right) = 2\epsilon_0 2\pi\lambda^2 = \frac{\phi_0^2}{\mu_0}. \tag{4.56}$$

Therefore, using Eqs. (4.46), (4.55) and (4.56), we finally obtain

$$U(y) = -\frac{\phi_0^2}{\mu_0} n_0 e^{-(2\pi l/3L_x)y}, \tag{4.57}$$

where n_0 is given by Eq. (4.43).

Eq. (4.57) gives us the external potential able to accommodate the vortices in a strictly conformal density profile. To simulate this, similar to the sawtooth potential used in the subsection 4.2.1, we model a periodic potential energy as the following (see Fig. 4.11.a)

$$U(y) = \begin{cases} -(n_0\phi_0^2/\mu_0)\, y/\tilde{\xi}, & 0 \leq y < \tilde{\xi}, \\ -(n_0\phi_0^2/\mu_0)\, e^{-(2\pi l/3L_x)(y-\tilde{\xi})}, & \tilde{\xi} \leq y < L, \end{cases} \tag{4.58}$$

where, in accordance with Eq. (4.43),

$$n_0 = \frac{N(2\pi l/3L_x)}{L_x[1 - e^{-(2\pi l/3L_x)(L-\tilde{\xi})}]}, \tag{4.59}$$

and $\tilde{\xi}$ is the width of the soft-wall represented by the first term of Eq. (4.58). As in our previously simulation, the value of $\tilde{\xi}$ was chosen in such a way that the maximum force exerted by the external potential is not enough to break the cooper pairs, which would locally invalidate the London approximation as well as induce the formation of vortex-antivortex pairs. Lastly, L is the length in which $U(y)$ is periodic, i.e., $U(y + L) = U(y)$. In what follows we assume $L = 60\lambda$.

The simulation consisted in repeating the same annealing process of the subsection 4.2.1, but now using the external potential presented in Eq. (4.58), where we chose $l = 3$ in order to fit the conformal map within the semiannular section (see Fig. 4.2). Fig. 4.11.a shows the vortex density profile obtained in the simulation and Fig. 4.10

shows the Voronoy diagram of the typical minimum energy configuration observed (in the physical z plane) and its correspondent inverse conformal mapping , given by $w(z) = (1/i\alpha)e^{i\alpha z}$, into the w plane (see Eq. (4.48)).

Observe that the vortex density profile fits well to the predicted conformal density profile (Eq. (4.46)), indeed, as shown in Fig. 4.10, under the chosen potential energy, the minimum energy vortex structure tends to form a strictly conformal crystal, except for some deformations.

Since the conformal mapping is given by an analytic function, the z and w planes are homeomorphic, i.e., the transformed conformal lattice preserves the same topological properties of the original hexagonal lattice. To analyse this in our simulations, we calculate the Euler characteristic, χ, which is a topological invariant, i.e., if two objects have the same topological properties they must also have the same value of χ. The Euler characteristic can be defined for a planar graph by the same formula as for polyhedral surfaces [60]

$$\chi = V - E + F, \tag{4.60}$$

where V, E, and F are respectively the numbers of vertices, edges and faces of the given structure. In Fig. 4.10(Top) we can observe that, even though the simulated structure presenting, locally, topological defects, the global Euler characteristic assumes the value $\chi = 0$, which is the same of the original hexagonal lattice.

For better identification we can define the local Euler characteristic, corresponding to each Voronoy cell as

$$\chi_{cell} = \frac{V}{3} - \frac{E}{2} + 1, \tag{4.61}$$

where we used the fact that each vertex of a Voronoy cell is shared with three cells, each edge is shared with two cells and each Voronoy cell has only one face. Therefore, the hexagonal, pentagonal and heptagonal cells have $\chi_{cell} = 0$, $\chi_{cell} = 1/6$ and $\chi_{cell} = -1/6$ respectively. Note that on the border the Voronoy cells are open. In this case the same reasoning of Eq.(4.61) is valid but we have to pay attention when using it. We can simply close the open polygons adding a new edge, in this case the new edge is not shared with any other cell and the two vertices connected by this edge are shared with only two cells. The Voronoy cells that present $\chi_{cell} \neq 0$ represent topological defects in the physical structure, called *disclinations* [61]. It is convenient to define the disclinations with $\chi_{cell} > 0$ and $\chi_{cell} < 0$ as, respectively, positive and negative topological charges.

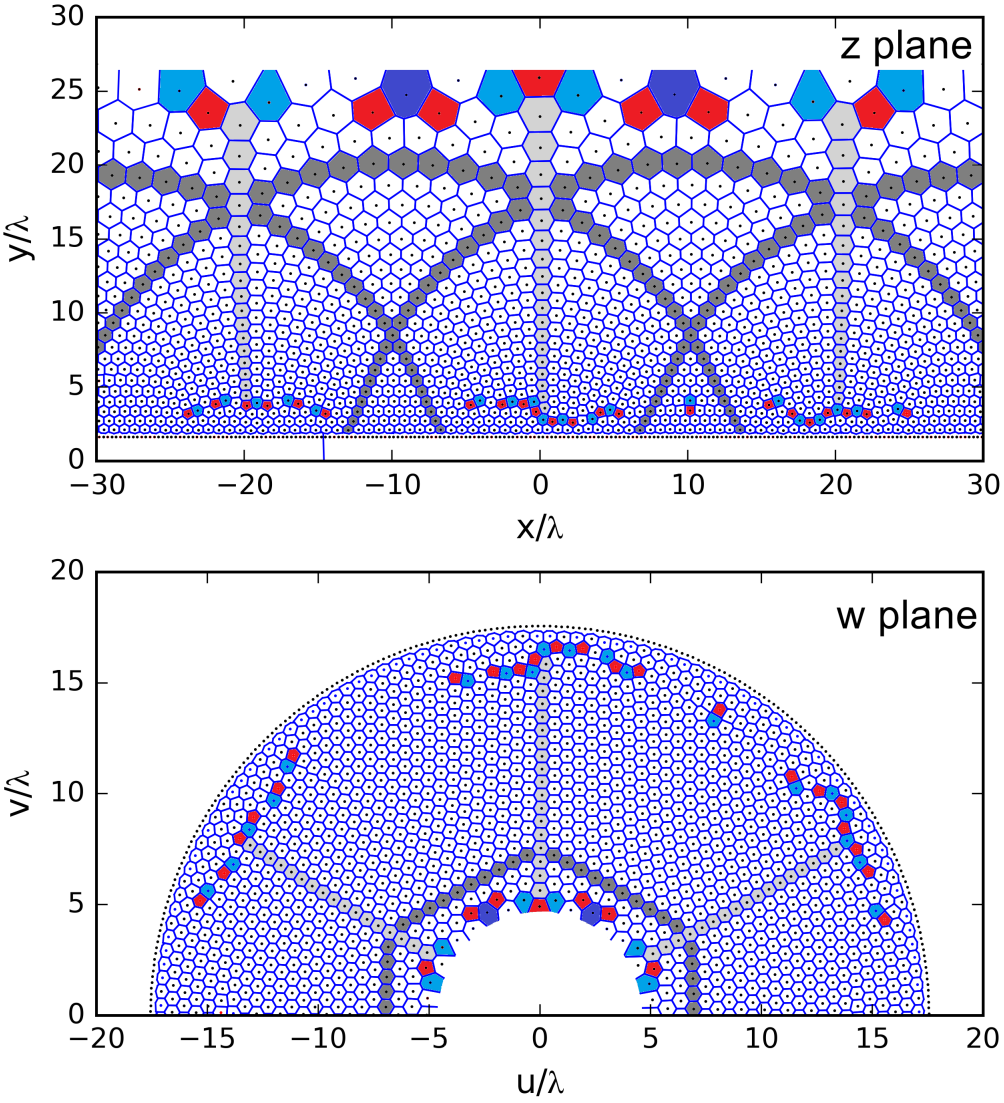

Figure 4.10: . Top: Voronoy diagram of the typical minimum energy configuration observed in the simulations (where it was translated in x direction by $\delta x = -6.7\lambda$ for a better visualization of the structure). Observe that the simulation result fits well with the chosen value of l and, for the chosen potential energy, the vortex structure organized in an almost strictly conformal crystal. The red, blue and purple shaded polygons represent, respectively, the Voronoy cells with $\chi_{cell} = 1/6$, $\chi_{cell} = -1/6$ and $\chi_{cell} = -2/6$ (see Eq. (4.61)). Observe that the global Euler characteristic is $\chi = \sum \chi_{cell} = 0$, which is the same of the original hexagonal lattice (the hexagonal cells have $\chi_{cell} = 0$ and are not shaded). The gray shaded polygons are guides to the eye for better identification of the arch and pillar structure of the conformal crystal. The lower border is topologically neutral, with pairs of positive and negative topological charges, which we are not showing. Bottom: Inverse conformal map of the physical z plane into the w plane. The vertical pillars and arches in the z plane are mapped into the w plane as, respectively, radial lines forming angles of 60° and the sides of a regular hexagon (where we shaded only the parts of the arches connecting the pillars).

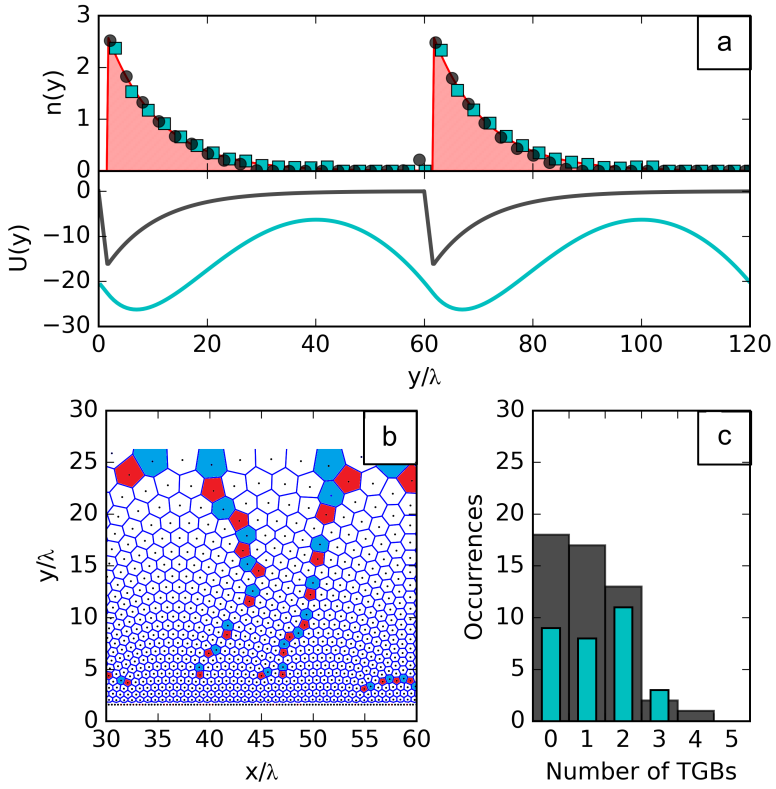

Figure 4.11: (a) Top: Vortex density profiles obtained in the simulations for bulk samples (circles) and thin films (squares). The area graph represents the expected exponential profile. Bottom: Potential energy profiles used in the the simulations (calculated from Eq. (4.54)) for the bulk (dark gray line) and thin-film (cyan line) cases (in the last one the energy profile was multiplied by a factor of 1/35 in order to better accommodate in the figure). (b) A typical conformal configuration, for the bulk case, exhibiting transverse grain boundaries (TGBs). (c) Distribution of the configurations obtained in the simulations for a bulk sample (gray bars) and a thin film (cyan bars) according to the number of TGBs.

Disclinations have a high energy cost and usually appear in pairs (dipoles of disclinations with same charge and opposite sign), called dislocations [61]. In Fig. 4.10 the Euler characteristic of each cell is identified by the color and the global Euler characteristic is given by $\chi = \sum \chi_{cell}$.

Now, let us discuss in more detail the configuration observed in Fig. 4.10 (Top). Among several realizations, all observed configurations presented the arches and pillars structure, but some of them are broken in domains separated by prominent, transverse grain boundaries (TGBs) [61], as illustrated in Fig. 4.11.b. These dislocation lines are topologically neutral (present $\chi = 0$) and cost little energy to be formed, such that it is difficult to determine which configuration is the ground state of the system. On the

other hand, as sketched in Fig. 4.11.c, among 50 different realizations of the annealing procedure we can observe that the single domain conformal vortex structure is the most frequent configuration and that the frequency of structures with more than two TGBs drops fast and represents less than one third of the configurations.

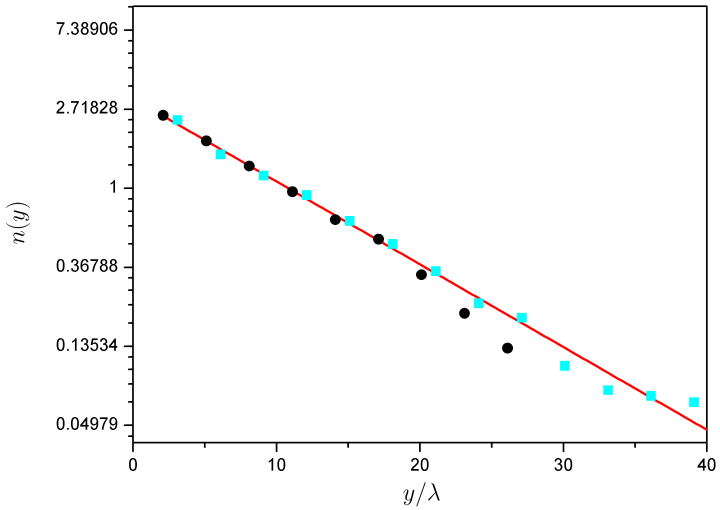

Figure 4.12: Semi-log graph of the vortex density profiles obtained in the simulations for bulk samples (circles) and thin films (squares). The red line represents the expected exponential profile.

Another behaviour that we observed in all configurations was that vortices close to the minimum of the external potential tend to form a conventional Abrikosov lattice with a principal axis aligned with the x axis (see Fig. 4.10). This compacted region has a width in the y direction of some vortex rows, where a transition between the Abrikosov and conformal lattices can be observed. In this Abrikosov-conformal transition, high-angle grain boundaries are always observed at the bottom of each pillar structure (greater deformation zones), where the hexagons suffer a sudden 30°-rotation between the conformal and Abrikosov domains. These high-angle grain boundaries, known as scars, are typical defect structures found in large $2D$ particle systems on curved surfaces [62–64] and each of them presents topological charge $\chi = 1/6$, which is conveniently cancelled by the topological charge located at the top of the same pillar structure, in order to preserve the global Euler characteristic.

Looking carefully at the configuration in the w plane [Fig. 4.10(Bottom)], one can notice that the area of the Voronoy cells becomes somewhat larger near the inner rim of the semiannular section. This unexpected behaviour is produced by topological defects present at the inner rim and reflects the failure of the density profile to follow precisely

the exponential shape (see Fig. 4.12), specially in the region correspondent to $y \geq 15\lambda$, where vortex spacings become larger than λ and the continuum approximation breaks down.

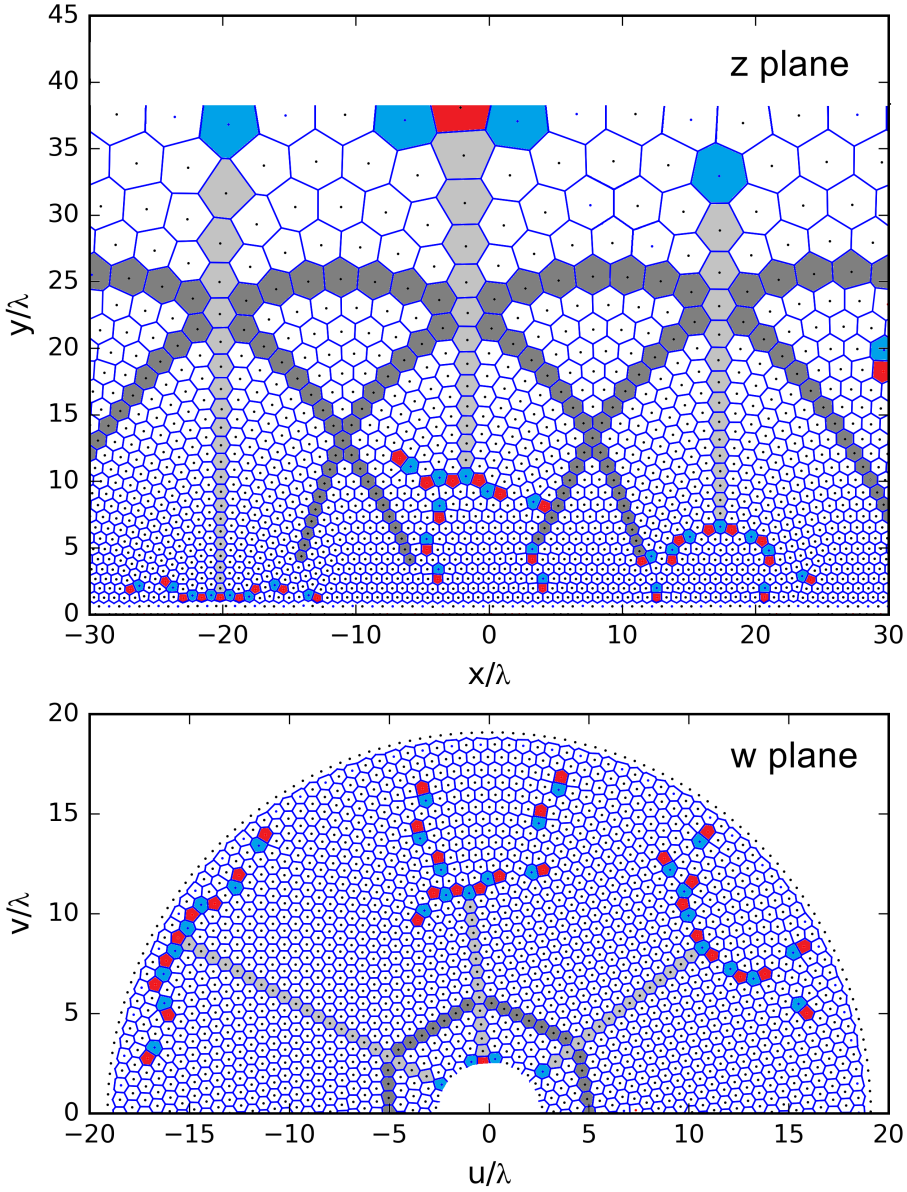

Figure 4.13: Top: Voronoy diagram of the typical minimum energy configuration observed in the thin film simulations. The shaded polygons are defined as the same of the Fig. 4.10. Bottom: Inverse conformal map of the physical z plane into the w plane. As in the bulk case, the vertical pillars and arches in the z plane are mapped into the w plane as, respectively, radial lines and the sides of a regular hexagon (where we shaded only the parts of the arches connecting the pillars).

As in the previously subsection, we also performed simulations for vortices in thin films. In this case the interaction potential becomes long range and we can not approximate the external potential by Eq. (4.55). In this case, we integrated Eq. (4.54) numerically for the specific vortex-vortex interaction potential, V_{int}, which can be calculated by integrating Eqs. (4.51), (4.52) [58]. The result, shown in Fig. 4.11.a, is remarkably different from the exponential energy profile used in the bulk case. The simulation result for the vortex density profile in thin films is also shown in Fig. 4.11.a., note that the observed density profile fits well to the required exponential profile.

Fig. 4.13 shows the Voronoy diagram of the typical minimum energy configuration observed in the thin film simulations and its correspondent inverse conformal mapping into the w plane. Apart from some visible deformations, the thin film results present the same arch-pillar configurations as in the bulk case. The topological charges also behaves similarly, with high angle grain boundaries located at the base of each pillar and subjected to the appearance of TGBs, in which the frequency (for 30 different realizations) is shown in Fig. 4.11.c. Note that, in the w plane the deformation in the area of the Voronoy cells near the inner rim is quite negligible compared with the bulk case. Indeed, the vortex density profile observed for thin films fits better with the expected exponential profile in the region $y \geq 15\lambda$ as compared to the bulk case (Fig. 4.12), since in the thin film case the distances between the particles are still much smaller than the range of the interaction potential and the continuous approximation is still valid. In general, the size of the Abrikosov regions observed to the thin film situations was larger than in the bulk cases. This may be a consequence of the strong correlation between the particles due to the long-range interaction potential, but a concrete explanation about this behaviour is still unclear for us. A study that could be done consists in repeat the same annealing procedure for particles interacting via power law pair potentials, using Eq. (4.54), and varying the exponent k (see Eq. (4.11)) to cover the long and short range domains and verify the appearance of Abrikosov regions.

4.2.3 Further results

In addition to the results presented above, we performed several simulations (the same annealing procedure) for different values of the parameters N and l, where the observed vortex structures presented, basically, the same characteristics as the structures presented above. However, for different values of l, specially for $l \geq 4$, the conformal density

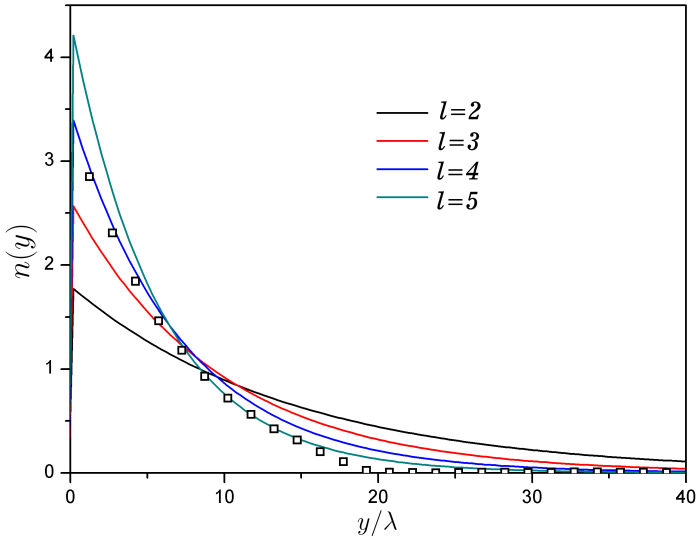

Figure 4.14: Lines: Expected conformal density profiles for for $N = 1500$ vortices in a simulation box of size $L_x = L_y = 60\lambda$. Squares: Example of the density profile observed in simulation for $l = 4$ in a bulk sample. Note that the density of vortices starts on the $l = 4$ curve and changes to the $l = 5$ curve. This is also a consequence of the violation of the continuum approximation (used in Eq. (4.55)) in the region $y \gtrsim 10\lambda$.

profiles are quite close (see Fig. 4.14), such that, occasionally, the vortex structure tries to accommodate in a deformed configuration between two conformal density profiles (see squares in Fig. 4.14). Fig. 4.15 shows an example of an observed structure, simulated for $l = 4$, that tries to accommodate five arches.

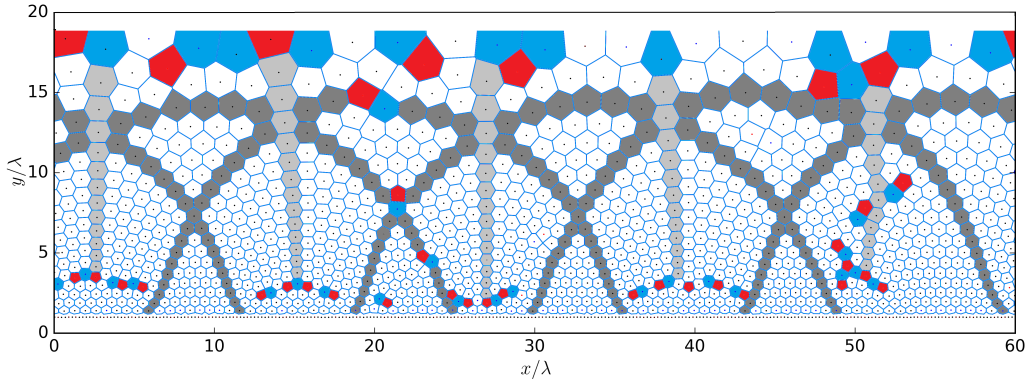

Figure 4.15: . Voronoy diagram of the simulation result (for $l = 4$) which density is sketched in Fig. 4.14. Note that , even though we have chosen $l = 4$, the observed configuration tries to form five arches.

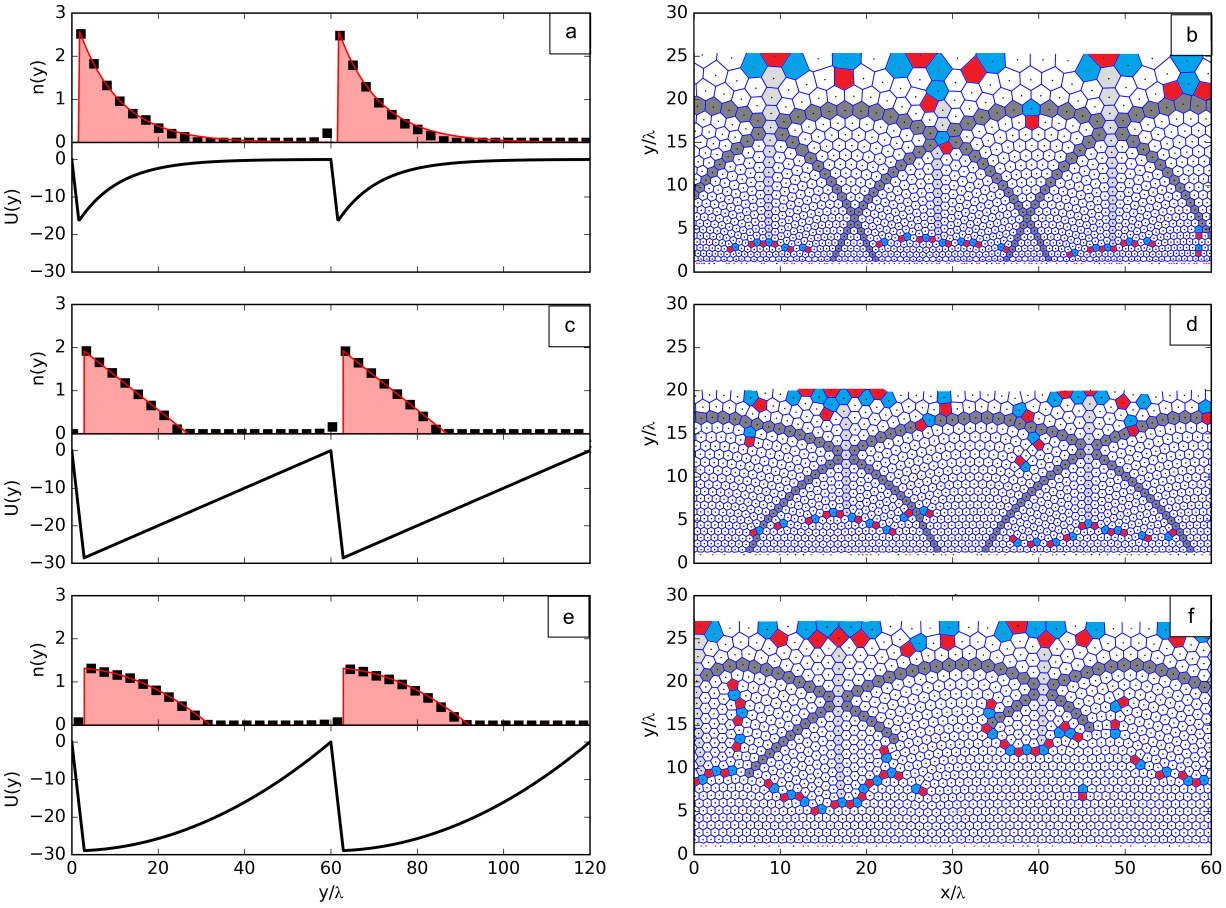

Figure 4.16: Left: Observed density profiles (top) and potential energy profiles (bottom) used in the simulations for the bulk case. Right: Voronoy diagram of the typical minimum energy configuration. (a) and (b): Results for the exponential potential (given by Eq. (4.58)), representing the external potentials with negative concavity. (c) and (d): Results for the linear potential (described in Fig. 4.7) . (e) and (f): Results for the parabolic potential (modeled for $U(y) = a + 0.05y + 0.008y^2$), representing the external potentials with positive concavity. The three potentials were chosen in such a way that the vortices were compressed in a region of approximately the same width in y direction $\approx 20\lambda$ against a soft-wall with the same inclination. The area graph represents the expected density profile for each external potential in accordance with Eq. (4.55).

The simulations also enable us to study the external potential shapes for which arcs and pillars structures appear. Fig. 4.16 shows three different results for external potentials in bulk superconductors representing the linear, positive concavity and negative concavity shapes. Observe that all of then, despite deformations, present the basic structure of pillars and arches. Therefore, one can conclude that this kind

of structure is a really comfortable and suitable configuration for nonuniform vortex distributions in a bulk superconductor.

4.2.4 Possible experimental realizations

Let us now briefly discuss the possibility of the experimental realization of conformal vortex crystals. At first, we basically need to find a way of reproduce the correct external potential able to accommodate the vortices in a conformal density profile. Since thin superconducting films are unable to screen magnetic fields, one can print flux-density textures directly into these systems using an external magnetic texture, this can be modelled by diverse procedures which have been explored exhaustively on the mesoscopic scale as a means of, for instance, enhancing flux pinning properties, generating vortex-antivortex patterns and manipulating vortex motion [65–67].

For observing conformal vortex systems it would be necessary to project a magnetic texture that resembles an exponential flux profile. In this case, since the density profile is determined by the external field profile, the necessary condition to maintain the conformal density profile would be automatically satisfied. Another possibility of inducing a nonuniform potential is by thickness modulation. However, in this case, the self energy and even the interaction energy of the vortices would depend on the local sample thickness, $d(r)$, and a more elaborated theory to relate the density of vortices to $d(r)$ would be necessary.

Fig. 4.17 presents a suggestion to reproduce a quasi-conformal vortex system in a bulk superconductor by reproducing the sawtooth external potential studied in the previous subsections (see Fig. 4.16.b), where the soft wall is represented by strong pinning planes and the compression force is given by a parallel applied current. The pinning planes could be formed by strong pinning materials, modelled by artificial pinning cites, or even represented by the so-called twin boundaries (TB), which are natural cracked lines in the material, where, in general, a large number of flux lines can be trapped. Maggio *et al, 1997* [68] studied the TB as barriers for the vortex motion (Fig. 4.17), where a field difference was imposed across a TB and the behaviour of the vortex rows was observed.

Applying an uniform current parallel to the TB (Fig. 4.18.a), a Lorentz force will arise, pushing the vortices toward the TB. This compression movement simulates the influence of a sawtooth external potential and may be able to form a vortex structure similar to

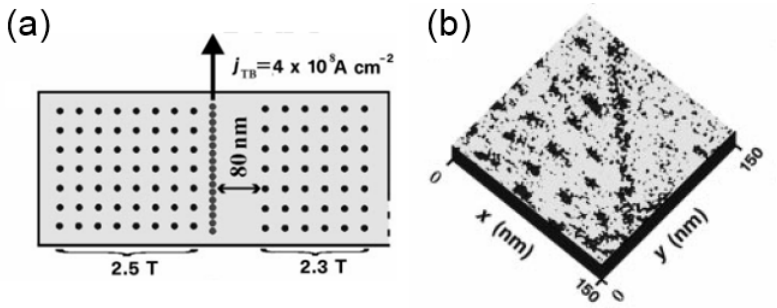

Figure 4.17: a) Simulation of the behaviour of rows of vortices distributed throughout two domains separated by a twin boundary filled with strongly pinned vortices. A field difference of $0.2T$ was imposed across the TB and the position of individual rows was determined by solving the London equation in an iterative process. J_{TB} is the screening current along the twin boundary. b) Spectroscopic image of the vortex lattice on the YBCO single-crystal surface at temperature $4.2k$, subjected to approximately the same field difference of (a). No more flux lines could be detected throughout the domain to the right over at least $80nm$. For more details see Maggio *et al, 1997* [68]. Figures taken from [68].

the gravity rainbow. To simulate this numerically, for the bulk case, we consider pinning lines positioned in $y_0 = 0$ and $y_0 = 60\lambda$ given by

$$U_p = -U_0 e^{(y-y_0)^2/2\xi^2}, \tag{4.62}$$

where we used $U_0 = 0.8\epsilon_0$, in a simulation box of size $L_x = 120\lambda$ x $L_y = 120\lambda$. Eq.(4.62) models, approximately, the twin boundary pinning potential (see e.g. Blatter, pag.*1323* [27]). The $N = 6000$ vortices were randomly distributed and an annealing procedure was done in order to find the uniform fundamental lattice (Abrikosov lattice). Particularly, along the pinning lines a large number of vortices were accumulated. Then, an uniform current $\mathbf{j} = 0.5\frac{\epsilon_0}{\phi_0\lambda}\hat{x}$ was applied, such that a Lorentz force $\mathbf{f} = -0.5\frac{\epsilon_0}{\lambda}\hat{y}$ emerged, compressing the vortices toward the TB. Fig. 4.18.c shows the typical observed vortex structure, where we allowed a thermal shaking (as in Eq. (4.49)) to help the system find the minimum energy state. Fig. 4.18.b shows the influence of the temperature in cleaning the topological defects.

The conformal structure is highly stable and we could observe it either by increasing the current gently or by relaxation after a quench.

Therefore, answering the questions formulated at the beginning of this chapter, we introduced the conformal crystals as possible ordered vortex structures in nonuniform density situations. We proposed a simple method to model a confining potential capable

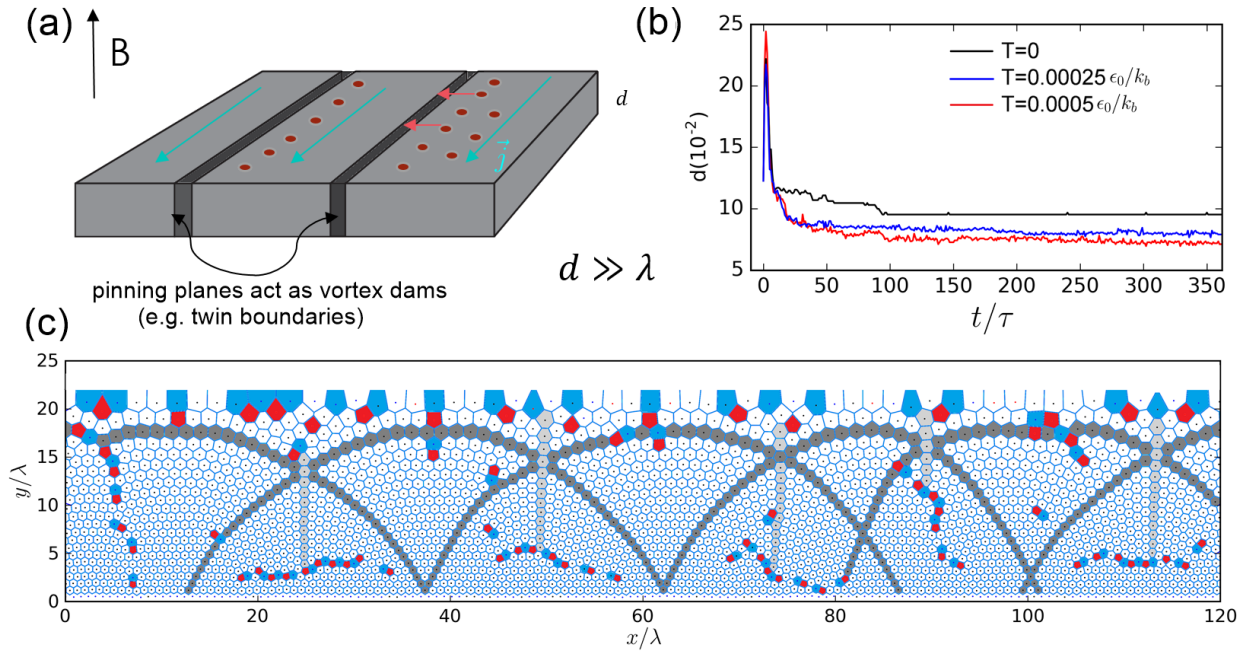

Figure 4.18: .a) schematic representation of the discussed experiment. The Lorentz force compresses the vortices in the pinning planes, resulting in a nonuniform vortex distribution as in the sawtooth potential simulations. b) Density of topological defects, d, observed in the vortex structure in function of time ($\tau = 10.000dt$) for different temperature values (used in the thermal shaking). When the current is turned on ($t = 0$), the lattice abruptly breaks in a kind of vortex soup and a high density of topological defects is observed. However, after a relaxation time the system tends to accommodate in the most orderly possible configuration. Note that the thermal shaking helps the system to eliminate the topological defects. c) Typical vortex structure observed in the simulations. All properties of this structure are similar to the sawtooth simulation case.

of accommodating conformal crystals in general, and showed that, under appropriate conditions, the conformal vortex crystal is an energetically favourable configuration.

5 Conclusion

We studied the effect of the surface barrier in the critical state problem and verified, using numerical simulations, which critical state model best describes the flux penetration profiles in a superconducting sample with random pinning distribution. In this situation we observed that the model of Kim (Kim et al,1963 [42, 43]) is the one which best describes the observed critical state profiles (see Fig. 3.7). Near the surfaces, we observed *vortex free regions*, which arise due to the energetic barrier that hinders the vortex entry and exit (J. Clem [45]). We introduced the dependence of the vortex free region thickness, x_{ff}, with the pinning potential (see Fig.3.8), where we observed that these regions are negligible for strong pinning, when the surface effects present little influence compared with the pinning forces. However, for weak pinning, these regions become relevant. In this case the magnetic flux density profile drops fast in a distance x_{ff} from the surfaces and follows the model of Kim for $x > x_{ff}$ (see Fig. 3.9). We also analysed the time evolution of the flux front position, x_p, for different pinning strength. We observed an initial time dependence of x_p as $x_p \propto t^{0.6}$, for all pinning values (see Fig. 3.10), which is close to the flux front temporal dependence, $t^{1/2}$, predicted by diffusion theory within our boundary conditions (Bryskin et al, 1993 [46]). The discrepancy in the flux front temporal dependence may be due to the surface barriers, not considered in Ref. [46]. However, a definitive answer for this question requires a more detailed study, not performed in this work. One possible attempt consists in simply simulate the same flux penetration process with and without the surface barrier and verify if the temporal dependence of x_p changes.

We also studied the conditions under which ordered structures in a nonuniform vortex distribution can be observed. We obtained evidence, using numerical simulations, of the formation of conformal vortex crystals, either in bulk superconducting samples or thin films. These ordered vortex structures, although can present local inhomogeneities, preserve the topological order and can be mathematically mapped into a triangular lattice through a conformal transformation. We proposed a simple method to obtain the potential energy capable of accommodating any arrangement of particles which interact

via a pair potential $V_{int}(r)$, in a conformal density distribution (see Eq.(4.54)). Such method is much more comprehensive than those ones used in the literature for mechanical equilibrium of conformal crystals (Rothen et al, 1996 [51]), where the expression obtained for the external force field capable of accommodating the conformal structure does not cover some important interaction laws, such as Coulomb interaction and logarithmic interaction, and is limited for power law interaction forces with $k > 2$ (see Eq.(4.37)). Eq.(4.54) can be applied in many situations, such as for colloids or systems of interacting particles in general. It can also be used to obtain other conformal structures, e.g, conformal crystals of radial symmetry. The conformal vortex crystals introduce a new range of possible ordered configurations for the vortex lattice beyond the well known Abrikosov lattice. Lastly, we suggested possible experimental realizations for obtaining conformal, or quasi conformal, vortex crystals in a superconductor, e.g., by compressing the vortex lattice against twin boundaries.

References

[1] H Kamerlingh Onnes. The resistance of pure mercury at helium temperatures. *Commun. Phys. Lab. Univ. Leiden*, 12(120), 1911.

[2] H Kamerlingh Onnes. *Leiden Comm.*, (133a), 1913.

[3] H Kamerlingh Onnes. *Leiden Comm.*, (139f), 1914.

[4] Walther Meissner and Robert Ochsenfeld. Ein neuer effekt bei eintritt der supraleitfähigkeit. *Naturwissenschaften*, 21(44):787–788, 1933.

[5] Fritz London and Heinz London. The electromagnetic equations of the supraconductor. In *Proceedings of the Royal Society of London A: Mathematical, Physical and Engineering Sciences*, volume 149, pages 71–88, 1935.

[6] VL Ginzburg. Zh. vl ginzburg and ld landau. *Zh. Eksp. Teor. Fiz*, 20:1064, 1950.

[7] H. Fröhlich. Theory of the superconducting state. i. the ground state at the absolute zero of temperature. *Phys. Rev.*, 79:845–856, 1950.

[8] John Bardeen, Leon N Cooper, and John Robert Schrieffer. Theory of superconductivity. *Physical Review*, 108(5):1175, 1957.

[9] Lev Petrovich Gor'kov. Microscopic derivation of the ginzburg-landau equations in the theory of superconductivity. *Sov. Phys. JETP*, 9(6):1364–1367, 1959.

[10] Paul M Chaikin and Tom C Lubensky. *Principles of condensed matter physics*, volume 1. Cambridge Univ Press, 2000.

[11] Charles P Poole Jr, Horacio A Farach, and Richard J Creswick. *Superconductivity.* Elsevier, 2007.

[12] Daniel Saint-James and PG de Gennes. Onset of superconductivity in decreasing fields. *Physics Letters*, 7(5):306–308, 1963.

[13] Robert Doll and M Näbauer. Experimental proof of magnetic flux quantization in a superconducting ring. *Physical Review Letters*, 7(2):51, 1961.

[14] Bascom S Deaver Jr and William M Fairbank. Experimental evidence for quantized flux in superconducting cylinders. *Physical Review Letters*, 7(2):43, 1961.

[15] A.A. Abrikosov. On the magnetic properties of superconductors of the second group. *Sov. Phys. JETP*, 5:1174, 1957.

[16] John R Clem. Simple model for the vortex core in a type ii superconductor. *Journal of low temperature physics*, 18(5-6):427–434, 1975.

[17] Pierre-Gilles De Gennes. *Superconductivity of metals and alloys*. Perseus Books Group, 1999.

[18] John Bardeen and MJ Stephen. Theory of the motion of vortices in superconductors. *Physical Review*, 140(4A):A1197, 1965.

[19] Ernst Helmut Brandt. The flux-line lattice in superconductors. *Reports on Progress in Physics*, 58(11):1465, 1995.

[20] Co Po Bean. Magnetization of hard superconductors. *Physical Review Letters*, 8(6):250, 1962.

[21] Michael Tinkham. *Introduction to superconductivity*. Courier Corporation, 1996.

[22] C. P. Bean. Magnetization of hard superconductors. *Phys. Rev. Lett.*, 8:250–253, 1962.

[23] D. LeBlanc and M. A. R. LeBlanc. ac-loss valley in type-ii superconductors. *Phys. Rev. B*, 45:5443–5449, 1992.

[24] Y. B. Kim, C. F. Hempstead, and A. R. Strnad. Critical persistent currents in hard superconductors. *Phys. Rev. Lett.*, 9:306–309, 1962.

[25] W. A. Fietz, M. R. Beasley, J. Silcox, and W. W. Webb. Magnetization of superconducting nb-25*Phys. Rev.*, 136:A335–A345, 1964.

[26] E Shimizu and D Ito. Critical current density obtained from particle-size dependence of magnetization in y ba 2 cu 3 o 7- δ powders. *Physical Review B*, 39(4):2921, 1989.

[27] Gianni Blatter, Mikhail V Feigel'man, Vadim B Geshkenbein, Anatoly I Larkin, and Valerii M Vinokur. Vortices in high-temperature superconductors. *Reviews of Modern Physics*, 66(4):1125, 1994.

[28] Ulsan National Institute of Science and Technology. https://phys.org/news/2015-03-d-nitrogenated-crystals-potential-rival.html.

[29] HF Hess, RB Robinson, RC Dynes, JM Valles Jr, and JV Waszczak. Scanning-tunneling-microscope observation of the abrikosov flux lattice and the density of states near and inside a fluxoid. *Physical review letters*, 62(2):214, 1989.

[30] RE Hetzel, A Sudbø, and DA Huse. First-order melting transition of an abrikosov vortex lattice. *Physical review letters*, 69(3):518, 1992.

[31] Surajit Sengupta, C Dasgupta, HR Krishnamurthy, Gautam I Menon, and TV Ramakrishnan. Freezing of the vortex liquid in high-t c superconductors: A density-functional approach. *Physical review letters*, 67(24):3444, 1991.

[32] Melissa Charalambous, Jacques Chaussy, Pascal Lejay, and Valerii Vinokur. Superheating of the abrikosov flux lattice. *Physical review letters*, 71(3):436, 1993.

[33] H Safar, PL Gammel, DA Huse, DJ Bishop, JP Rice, and DM Ginsberg. Experimental evidence for a first-order vortex-lattice-melting transition in untwinned, single crystal yba 2 cu 3 o 7. *Physical review letters*, 69(5):824, 1992.

[34] Eli Zeldov, D Majer, Marcin Konczykowski, Vadim B Geshkenbein, et al. Thermodynamic observation of first-order vortex-lattice melting transition in bi2sr2cacu2o8. *Nature*, 375(6530):373, 1995.

[35] I Guillamón, H Suderow, A Fernández-Pacheco, J Sesé, R Córdoba, JM De Teresa, MR Ibarra, and S Vieira. Direct observation of melting in a two-dimensional superconducting vortex lattice. *Nature Physics*, 5(9):651–655, 2009.

[36] Frederick A Lindemann. Ueber die berechnung molekularer eigenfrequenzen. *Phys. Z*, 11:609–612, 1910.

[37] Erwin Frey, David R Nelson, and Daniel S Fisher. Interstitials, vacancies, and supersolid order in vortex crystals. *Physical Review B*, 49(14):9723, 1994.

[38] Oskar Karl Gustav Tietjens and Ludwig Prandtl. *Applied hydro-and aeromechanics: based on lectures of L. Prandtl*, volume 2. Courier Corporation, 1957.

[39] John David Jackson. *Classical electrodynamics*. Wiley, 1999.

[40] C. P. Bean and J. D. Livingston. Surface barrier in type-ii superconductors. *Phys. Rev. Lett.*, 12:14–16, 1964.

[41] B. Raes, C. C. de Souza Silva, A. V. Silhanek, L. R. E. Cabral, V. V. Moshchalkov, and J. Van de Vondel. Closer look at the low-frequency dynamics of vortex matter using scanning susceptibility microscopy. *Phys. Rev. B*, 90:134508, 2014.

[42] Y. B. Kim, C. F. Hempstead, and A. R. Strnad. Magnetization and critical supercurrents. *Phys. Rev.*, 129:528–535, 1963.

[43] Y. B. Kim, C. F. Hempstead, and A. R. Strnad. Resistive states of hard superconductors. *Rev. Mod. Phys.*, 36:43–45, 1964.

[44] R. A. Richardson, O. Pla, and F. Nori. Confirmation of the modified bean model from simulations of superconducting vortices. *Phys. Rev. Lett.*, 72:1268–1271, 1994.

[45] John R. Clem. A model for flux pinning in superconductors. *Low Temperature Physics*, 3:102, 1974.

[46] VV Bryskin and SN Dorogotsev. Space-time image of the magnetic flux penetrating into type-ii superconductors in an applied oscillating magnetic field. *Physica C*, 215:173, 1993.

[47] John Gilchrist and CJ Van der Beek. Nonlinear diffusion in hard and soft superconductors. *Physica C: Superconductivity*, 231(1):147–156, 1994.

[48] André A Moreira, José S Andrade Jr, Josué Mendes Filho, and Stefano Zapperi. Boundary effects on flux penetration in disordered superconductors. *Physical Review B*, 66(17):174507, 2002.

[49] Piotr Pieranski. Gravity's rainbow- structure of a 2d crystal grown in a strong gravitational field. *Phase Transitions in Soft Condensed Matter*, 211:45–48, 1989.

[50] F Rothen, Piotr Pieranski, N Rivier, and A Joyet. Cristaux conformes. *European journal of physics*, 14(5):227–233, 1993.

[51] François Rothen and Piotr Pierański. Mechanical equilibrium of conformal crystals. *Physical Review E*, 53(3):2828, 1996.

[52] Krzysztof W Wojciechowski and Jaroslaw Klos. On the minimum energy structure of soft, two-dimensional matter in a strong uniform field:gravity's rainbow'revisited. *Journal of Physics A: Mathematical and General*, 29(14):3963, 1996.

[53] W Drenckhan, D Weaire, and SJ Cox. The demonstration of conformal maps with two-dimensional foams. *European journal of physics*, 25(3):429, 2004.

[54] A Mughal and MA Moore. Topological defects in the crystalline state of one-component plasmas of nonuniform density. *Physical Review E*, 76(1):011606, 2007.

[55] James Ward Brown, Ruel Vance Churchill, and Martin Lapidus. *Complex variables and applications*, volume 7. McGraw-Hill New York, 1996.

[56] D Ray, C Reichhardt, and CJ Olson Reichhardt. Pinning, ordering, and dynamics of vortices in conformal crystal and gradient pinning arrays. *Physical Review B*, 90(9):094502, 2014.

[57] Clécio Clemente de Souza Silva. *Propriedades de equilíbrio e de transporte da matéria de vórtices em nanoestruturas supercondutoras*. PhD thesis, Universidade Federal de Pernambuco, 2003.

[58] Niels Grønbech-Jensen. Summation of logarithmic interactions in periodic media. *International Journal of Modern Physics C*, 7(06):873–881, 1996.

[59] Linda E. Reichl. *A Modern Course in Statistical Physics*. Wiley, 2016.

[60] David S Richeson. *Euler's gem: the polyhedron formula and the birth of topology*. Princeton University Press.

[61] Philip Kim. Graphene: Across the border. *Nature materials*, 9(10):792–793, 2010.

[62] AR Bausch, MJ Bowick, A Cacciuto, AD Dinsmore, MF Hsu, DR Nelson, MG Nikolaides, A Travesset, and DA Weitz. Grain boundary scars and spherical crystallography. *Science*, 299(5613):1716–1718, 2003.

[63] William TM Irvine, Vincenzo Vitelli, and Paul M Chaikin. Pleats in crystals on curved surfaces. *Nature*, 468(7326):947–951, 2010.